CHEMISTRY
A EUROPEAN JOURNAL

DOI: 10.1002/chem.200600135

$Pd_{0.213}Cd_{0.787}$ and $Pd_{0.235}Cd_{0.765}$ Structures: Their Long *c* Axis and Composite Crystals, Chemical Twinning, and Atomic Site Preferences

Joshua Teal Schmidt,[a] Stephen Lee,*[a] Daniel C. Fredrickson,[a] Matthias Conrad,[b] Junliang Sun,[a] and Bernd Harbrecht[b]

Abstract: We present single-crystal studies of $Pd_{0.213}Cd_{0.787}$ and $Pd_{0.235}Cd_{0.765}$, synchrotron powder studies of $Pd_{1-x}Cd_x$, $0.755 \geq x \geq 0.800$, and LDA-DFT and extended Hückel (eH) calculations on these or related phases. The two single-crystal structures have *a*, *b*, and *c* axis lengths of 9.9013(7), 14.0033(10), 37.063(24) and 9.9251(3), 14.0212(7), 60.181(3) Å, respectively and they crystallize in the space groups *Ccme* and *F2mm*, respectively (solved as (3+1)-dimensional crystals their most convenient superspace group is $Xmmm(00\gamma)s00$). The structures have two different structural components each with their own separate axis parameters. Powder data shows that the ratio of these separate axes (*S*/*L*) varies from 1.615 to 1.64, values near the golden mean (1.618). For $Pd_{0.213}Cd_{0.787}$, different Pd and Cd site occupancies lead to variation in the *R* factor from 2.6–3.6%. The site occupancy pattern with the lowest *R* factor (among the 26820 variants studied) is the exact site occupancy pattern predicted by LDA-DFT parameterized eH Mulliken charge populations. The phases can be understood through a chemical twinning principle found in γ-brass, the parent structure for the above phases (a relation with the $MgCu_2$ Laves phase is also noted). This twinning principle can be used to account for Cd and Pd site preferences. At the same time there is a clean separation among the Cd and Pd atoms for the two separate chain types at height $b = 0$ and 1/2. These results indicate that Cd:Pd stoichiometry plays a role in phase stability.

Keywords: cadmium · intermetallic phases · palladium · solid-state structures · X-ray crystallography

Introduction

Although we tend to think of polymers and biological systems as having the largest, and hence the most complex, of crystal structures,[1,2] an examination of unit cell lengths among the disparate subfields of chemistry reveals that among the largest, if not the largest of unit cells, are some intermetallic solids.[3–11] In recent years, the origin of some large intermetallic structures have become clear within the framework of quasicrystals and quasicrystalline approximants.[12,13] However, the literature still abounds with large unit-celled intermetallic crystals not understood in the quasicrystalline framework.[8–10,14–19]

The largest of the intermetallic structures, as yet unconnected with quasicrystalline phases, are binary structures from Groups 10–12 in the periodic table. An example of these is γ-$Cu_{1-x}Zn_x$ ($0.586 < x < 0.60$), an apparently trigonal or hexagonal phase with an *a* axis of some 2000 Å.[10,20] And closely associated to this phase are the orthorhombic phases $Cu_{1-x}Zn_x$, $56.5 \geq x \geq 58.6$, which have long axes that reach more than 100 Å.[20]

We concentrate in this paper on this last type of orthorhombic phase. Since the initial discovery of these phases by electron diffraction 30 years ago,[20–22] other researchers have also studied these systems.[23,24] A single-crystal structure of the closely related $NiZn_3$ phase has been published.[9] Pictures of a structural model based on electron diffraction data are known.[25] Abstracts, without atomic coordinates or diagrams, of other single-crystal structures have also appeared.[26] We summarize the literature with the following picture: that Group 10 and Group 12 or Group 11 and Group 12 elements produce orthorhombic binary structures closely related to the γ-brass structure, that there is a rela-

[a] Dr. J. T. Schmidt, Prof. Dr. S. Lee, Dr. D. C. Fredrickson, Dr. J. Sun
Department of Chemistry and Chemical Biology
Baker Laboratory, Cornell University, Ithaca
NY 14853–1301 (USA)
E-mail: sl137@cornell.edu

[b] Dr. M. Conrad, Prof. Dr. B. Harbrecht
Department of Chemistry and Center of Material Sciences
Philipps University Marburg, 35032 Marburg (Germany)
Fax: (+1) 607-255-4137

Supporting information for this article is available on the WWW under http://www.chemeurj.org/ or from the author.

tion between the number of valence electrons and the cell axes, and that the variation in axis length can be understood by a nearly free electron model.[8,20,21,24,27,28]

In this paper, we present structural models for two single-crystal structures in the $Pd_{1-x}Cd_x$ system, a detailed synchrotron powder diffraction study for $Pd_{1-x}Cd_x$, $0.755 \geq x \geq 0.800$, and LDA-DFT and semiempirical band calculations on these same or related systems. Our results confirm that the long axis of $Pd_{1-x}Cd_x$ orthorhombic phases is related to the γ-brass structure. However, the results given alter our understanding of the relation between the number of valence electrons and the cell axes.

We find that $Pd_{1-x}Cd_x$, $0.755 \geq x \geq 0.800$ phases are more properly thought of as composite crystals. Composite structures are structures in which the full crystal structure can be decomposed into two separate pieces, each with their own fundamental unit-cell lattice parameters.[29–32] In the case of $Pd_{1-x}Cd_x$, $0.755 \geq x \geq 0.800$ phases, the two separate units involve chains of atoms with different interatomic spacings. These spacings are described by dividing the long axis into an integer number of segments (S and L). We find that the Cd/Pd ratio does not govern the long axis length in any simple manner, rather it controls both the S/L ratio and the chemical twinning planes (this twinning law is described in detail later).

These results are surprising. We might have expected that like γ-brass, which is an electron phase,[33–37] there would be a direct correlation between the number of states at the Fermi energy and the number of valence electrons in the phase. Both the single-crystal structures and the band calculations reported in this paper contradict this view. Instead, our band calculations show no direct correlation between experimental electron filling and the number of states at the Fermi energy. They show instead that the primary feature of these phases is an electron depopulation along the S chains and conversely electron accumulation along the L chains. These electronic effects correlate to Cd and Pd site preferences and the twinning pattern in the various structures.

Experimental Section

Synthesis and microprobe: The $Pd_{0.235}Cd_{0.765}$ and $Pd_{0.213}Cd_{0.787}$ bulk samples were prepared by combining palladium powder (Aldrich, 99.9%, 200 mesh) and cadmium foil (Aldrich, 99.99+%, 0.5 mm thick) in the appropriate mass ratios targeting 400 mg of product in an evacuated quartz glass tube, which had been flushed with argon gas. The $Pd_{0.235}Cd_{0.765}$ sample was heated to 820 °C over 5 h and then was slow cooled to 400 °C over two weeks before being allowed to cool to room temperature. The $Pd_{0.213}Cd_{0.787}$ sample was heated to 800 °C over 5 h, held at 800 °C for 12 h, cooled to 600 °C over 400 h, cooled to 400 °C over 100 h, and then allowed to cool to room temperature by shutting off the furnace.

By powder data, we confirmed that both the S/L ratio 13:8 and 21:13 structures (the two structures reported in this paper) can be prepared in quantitative yield. Calculated and experimental powder patterns for $Pd_{0.213}Cd_{0.787}$ and $Pd_{0.235}Cd_{0.765}$ are given in the Supporting Information. These results confirm that the former compound corresponds to a 13:8 and the latter a 21:13 system. Also given in the Supporting Information are the average error in 2θ as a function of S/L for the two systems; these results confirm the reported values of S/L. The $Pd_{0.213}Cd_{0.787}$ composition is the exact one from which the 13:8 single crystal was chosen. For the 21:13 system, a powder sample with nominal composition $Pd_{24.0}Cd_{76.0}$ was used, which is only slightly different to the nominal stoichiometry of the 21:13 single-crystal sample. The powder data for both systems (synchrotron) does not show the presence of any additional crystalline phases.

The other Pd/Cd samples discussed later in the section on S/L as a function of x were prepared by combining the elements in evacuated, sealed quartz glass ampules and then heating to 925 °C over 5 h, holding at 925 °C for 5 h, cooling to 445 °C over 600 h, cooling to 400 °C over 24 h, and then allowing to cool to room temperature by shutting off the furnace.

The sample with the nominal composition $Pd_{0.235}Cd_{0.765}$ was characterized with the JEOL 8900 EPMA Microprobe at the Cornell Center for Materials Research (CCMR). Five separate measurements were taken on each of two distinctly different samples to establish a standard deviation (the result was $Pd_{0.226(5)}Cd_{0.774(5)}$, within two standard deviations of the nominal composition reported here). For the sample with the nominal composition $Pd_{0.213}Cd_{0.787}$, microprobe measurement was performed on the same single crystal used for the X-ray diffraction data collection. Three measurements were taken to establish a standard deviation (the result was $Pd_{0.216(3)}Cd_{0.784(3)}$, within one σ of the nominal composition). As nominal compositions are close to the results of microprobe data, and as no additional crystalline phase was observed in the synchrotron powder pattern, the nominal composition values are used as phase names throughout this paper.

Single-crystal data: A single crystal of $Pd_{0.235}Cd_{0.765}$ was selected from the bulk sample and was shattered by mortar and pestle; this sample was then used for X-ray data collection. The data collection and structure refinement details are given in Table 1. The atomic positions and isotropic thermal parameters are given in Table 2. The anisotropic thermal parameters are given in the Supporting Information. After the atomic positional and thermal parameters had refined to their optimal value, the site occupancy factors (s.o.f.) were allowed to refine and found to vary no more than 3% from full occupancy. We therefore report here a full occupancy model of the crystal. This orthorhombic crystal was determined to be F-centered, there were no observed diamond glide absence laws, the R factor was 4.7%, and structure refinement was routine in space group $F2mm$. The $F2mm$ model is noncentrosymmetric. To understand why the centrosymmetric $Fmmm$ is not allowed in this case, we note that the $F2mm$ model is a superstructure of γ-brass (Cu_5Zn_8). The γ-brass structure is based on two nested tetrahedra, an inner tetrahedron (IT) and an outer tetrahedron (OT). In the $Pd_{0.235}Cd_{0.765}$ superstructure the inner and outer tetrahedra are oriented with a twofold axis along the a direction. This orientation of the IT and OT forbids a mirror plane normal to the a axis. Thus, the centrosymmetric $Fmmm$ and other noncentrosymmetric space groups with a mirror plane in the first setting ($Fm2m$ and $Fmm2$) are forbidden by this observation.

A single crystal of $Pd_{0.213}Cd_{0.787}$ was selected in the same fashion and an X-ray data set was collected on it. The data collection and structure refinement details are also given in Table 1, while the atomic positions and isotropic thermal parameters are given in Table 3. The anisotropic thermal ellipsoids are given in the Supporting Information. As before, the s.o.f. were allowed to refine after the optimal positional and thermal parameters were determined and found to vary no more than 5% from full occupancy. Again, we report a full occupancy model here. The R factor of the refinement was 2.6%. While the structure refinement itself was routine, the determination of systematic absences required a more detailed analysis than that provided by ordinary analysis software (XPREP).[38] The program XPREP strongly suggested the noncentrosymmetric space group $C2me$. A review of the reflections data file showed that this assignment was based upon a few low intensity $0kl$ (with l odd) peaks with wildly varying measured intensity values. For the determination of systematic absences, instead of determining peak standard deviations based upon background measurements, we directly calculated standard deviations of all peaks with multiple measurements (i.e., three or more measurements). We considered only reflections with $I > 2\sigma(I)$ in the

Table 1. Data collection and structure refinement parameters for $Pd_{0.213}Cd_{0.787}$ and $Pd_{0.235}Cd_{0.765}$.

	$Pd_{0.213}Cd_{0.787}$	$Pd_{0.235}Cd_{0.765}$
formula	$Pd_{59}Cd_{217}$	$Pd_{105}Cd_{343}$
space group	*Ccme* (No. 64)	*F*2*mm* (No. 42)
Z	1	1
a [Å]	9.9013(7)	9.9251(3)
b [Å]	14.0033(10)	14.0212(7)
c [Å]	37.0630(24)	60.181(3)
V [Å^3]	5138.8(8)	8374.9(12)
ρ_{calcd} [g cm^{-3}]	9.910	9.834
μ [mm^{-1}]	26.880	26.613
data collection		
crystal size [mm^3]	$0.2\times0.1\times0.05$	$0.12\times0.05\times0.025$
θ range [°]	1.10–35.28	0.67–30.67
crystal color	metallic silver	metallic silver
diffractometer	X8 APEX (Bruker)	Smart 1 K (Bruker)
T [K]	180	180
radiation	$Mo_{K\alpha}$	$Mo_{K\alpha}$
index range	$-10\le h\le 15$	$-13\le h\le 13$
	$-20\le k\le 22$	$-19\le k\le 14$
	$-59\le l\le 52$	$-84\le l\le 62$
reflections collected	43751	17179
data reduction		
program	SAINT,[112] X-RED[113]	SAINT ,[112] X-RED[113]
absorption correction	X-SHAPE[114]	X-SHAPE[114]
unique reflections/R_{int}	5786/0.0630	5749/0.0745
refinement		
programs	SHELXS-, -XL-97[60]	SHELXS-, -XL-97[60]
variables	174	286
observed reflns [$I_o>4\sigma(I_o)$]	3007	3188
R_1 [$I_o>4\sigma(I_o)$]/R_1 (all)	0.0259/0.0489	0.0465/0.0909
wR_2/goodness of fit	0.0728/0.820	0.1149/1.007
extinction coefficient	0.000095(3)	0.000079(3)
largest diff. peak/hole [e Å^{-3}]	2.001/−2.140	2.900/−2.234

five orthorhombic point groups *mmm*, 2*mm*, *m*2*m*, *mm*2, and 222, which each have several thousand unique reflections that meet these criteria. Considering only those systematic absences that go beyond C-centering (the data was integrated assuming this centering condition) there proved to be clean systematic absences for 0*kl*, with *l* odd and *hk*0, with either *h* or *k* odd (counting only those peaks with intensity > 1/2000 of the most intense peak). This was consistent with the reported *Ccme* space group. The structure proves to be a twinned γ-brass structure; the two twinned components are connected to one another by the *c* glide in the first setting.

Powder data: Synchrotron X-ray radiation from beamline X3B1 at the National Synchrotron Light Source was used to record powder patterns. The samples were ground in an agate mortar and pestle, passed through a 270 mesh sieve and then placed on an off-cut quartz sample holder. Powder patterns were recorded with a 0.005° step in the detector. For each step, the sample holder was rotated 3°.

Indexing of powder data followed a procedure slightly more complex than usual as it proved possible to fit an additional parameter (i.e., *S*/*L*) beyond the normal cell parameters. This parameter is the ratio between the interatomic spacing of two different chains in the structure. (The two different chains divide the orthorhombic *c* axis into *S* and *L* segments. If the ratio *S*/*L* is a rational fraction, then the structure is commensurate; if it is irrational, the structure is incommensurate.)

The essential idea behind powder refinement of the *S*/*L* parameter becomes clear if one examines powder patterns of the four single-crystal structures which we have solved in the $Pd_{1-x}Cd_x$ family. A region of these patterns is shown in Figure 1. (Besides the two single-crystal structures reported in this paper, we also include $Pd_{21.1}Cd_{78.9}$ ($S=31$, $L=19$) and $Pd_{20.4}Cd_{79.6}$ ($S=18$, $L=11$) in this figure. While these two structures are not yet in their fully final form, their refined *R* factors of 4.83% and 5.04% suggest their suitability in analyzing the powder data.)

As Figure 1 shows, there is a continuous evolution of peak positions in the four patterns. Peaks that are related to one another are indicated by the small grey ellipses. Such evolution is found not just in the region shown in Figure 1, but across the full powder pattern as well. The relation between peaks extends to peak indexation as well. While the *h* and *k* indices remain constant across series of related peaks, the *l* index varies as a function of the *S* and *L* parameters. For the four sets of peaks illustrated by ellipses in Figure 1 the (*hkl*) indices are (240), (203*L*−*S*), (11*S*) and (223*L*−*S*). The *S* and *L* values of a given structure are given on the left of Figure 1.

In order to find the value of *S*/*L* that fits best the experimental powder pattern, we used a least-squares procedure. As in ordinary refinement, we needed to establish those peaks for which there is no doubt as to their *hkl* values. In ordinary refinement, one does so by comparing to a known single-crystal structure. Here, we had to examine a continuous range of structures. We choose the range of *S*/*L* from 21/13 = 1.615 to 18/11 = 1.637, this range being the range of our existing single-crystal solutions. Our method was therefore only correct for powder patterns the refined *S*/*L* parameters of which prove to be between the above-mentioned values.

We tabulated, for the four single-crystal structures, the range of 2θ values of all diffraction peaks with intensities greater than or equal to 0.25% of the most intense peak (this master list is given in the Supporting Information). We then considered a particular powder data set. We examined the given powder pattern for all peaks that experimentally look to be non-overlapping peaks (intensity $\ge 3\sigma$, $\ge 0.1°$ from nearest other peak, and experimentally fit as a single peak). We compared the so-generated list with the earlier obtained master list. We considered only those experimental peaks in the given data set which by the master list were in the range of only a single *hkl* reflection. In Table 4 an example is given of such a list for the $Pd_{0.213}Cd_{0.787}$ sample. As Table 4 shows, for this sample, only 11 reflections meet all the specified criteria.

We then used ordinary three-dimensional crystal cell refinement to determine cell parameters. However, instead of refining the cell parameters for a fixed *S* and *L* value, we chose all *S* and *L* parameters with an *S*/*L* range from 21/13 = 1.615 to 18/11 = 1.637 and for which the *S* value was less than or equal to 100 (an *S* value of 100 corresponds to a unit cell of over 250 Å, beyond the comfortable resolution limit for single-crystal diffractometers). The average error between observed and calculated 2θ values proved to be a function of *S*/*L*. The average errors for the $Pd_{0.213}Cd_{0.787}$ sample are shown in Figure 2. As this figure shows, this function reached a minimum for the *S*/*L* value of 13:8 = 1.625 with an average error of 0.0027°, less than the motor step size on the detector used. This method proved to give similar results for all the powder data reported in this paper.

Table 2. Positional and thermal parameters for $Pd_{0.235}Cd_{0.765}$.

Atom[a]	*x*/*a*	*y*/*b*	*z*/*c*	s.o.f.	U_{eq} [Å^2]
M1	0.0017(3)	0	0.4612(1)	1	0.010(1)
M2	0.5097(4)	0	0.3461(1)	1	0.011(1)
M3	0.5171(3)	0	0.2697(1)	1	0.011(1)
M4	0.3404(3)	0.6739(3)	0	1	0.012(1)
M5	0.4956(3)	0	0.4229(1)	1	0.012(1)
M6	0.6772(2)	0.8238(2)	0.1913(1)	1	0.010(1)
M7	0.8429(2)	0.6748(2)	0.1170(1)	1	0.013(1)
M8	0.9907(4)	0	0.3076(1)	1	0.012(1)
M9	0.0287(3)	0	0.3851(1)	1	0.010(1)
M10	0.0269(4)	0	0	1	0.010(1)
M11	0.6744(2)	0.6761(2)	0.0744(1)	1	0.009(1)
M12	0.8480(2)	0.8237(2)	0.2339(1)	1	0.015(1)
M13	0.6664(2)	0.8212(2)	0.0425(1)	1	0.012(1)
M14	0.3055(4)	0	0	1	0.007(1)
M15	0.7076(3)	0	0.3089(1)	1	0.017(1)
M16	0.8526(2)	0.8230(2)	0.1486(1)	1	0.014(1)
M17	0.3064(3)	0	0.3819(1)	1	0.011(1)
M18	0.6603(2)	0.6781(2)	0.1597(1)	1	0.012(1)
M19	0.2118(3)	0	0.4270(1)	1	0.013(1)
M20	0.8614(2)	0.6790(2)	0.0325(1)	1	0.014(1)
M21	0.6494(2)	0.6798(2)	0.2241(1)	1	0.016(1)
M22	0.7979(3)	0	0.2625(1)	1	0.017(1)
M23	0.8760(2)	0.8155(2)	0.0822(1)	1	0.018(1)
M24	0.0144(3)	0.3740(2)	0.1534(1)	1	0.018(1)
M25	0.4886(3)	0.6255(2)	0.0397(1)	1	0.014(1)
M26	0.8866(2)	0.8113(2)	0.3061(1)	1	0.016(1)
M27	0.1364(3)	0.3149(2)	0.1115(1)	1	0.018(1)
M28	0.0394(3)	0.8788(2)	0.2682(1)	1	0.016(1)
M29	0.1299(3)	0.8137(3)	0	1	0.014(1)
M30	0.7208(3)	0	0.4534(1)	1	0.015(1)
M31	0.9655(2)	0.6188(2)	0.0758(1)	1	0.015(1)
M32	0.7896(3)	0	0.3571(1)	1	0.013(1)
M33	0.0577(2)	0.1146(2)	0.1161(1)	1	0.012(1)
M34	0.0605(3)	0.6107(3)	0	1	0.011(1)
M35	0.9559(2)	0.8884(2)	0.1914(1)	1	0.015(1)
M36	0.2311(3)	0	0.3343(1)	1	0.014(1)
M37	0.2788(3)	0	0.4760(1)	1	0.013(1)
M38	0.2466(3)	0	0.2858(1)	1	0.017(1)
M39	0.7644(4)	0	0.4047(1)	1	0.014(1)

[a] Structure refined with M1–M11: Pd and M12–M39: Cd.

Table 3. Positional and thermal parameters for $Pd_{0.213}Cd_{0.787}$.

Atom[a]	*x*/*a*	*y*/*b*	*z*/*c*	s.o.f.	U_{eq} [Å^2]
M1	0.2414(1)	0	0.2186(1)	1	0.008(1)
M2	0.2467(1)	0	0.0931(1)	1	0.007(1)
M3	0.5826(1)	0.1747(1)	0.1550(1)	1	0.008(1)
M4	0.2664(1)	0	0.9689(1)	1	0.008(1)
M5	0.9155(1)	0.8245(1)	0.0345(1)	1	0.007(1)
M6	0.7693(1)	0	0.1564(1)	1	0.007(1)
M7	0.4121(1)	0.1772(1)	0.2237(1)	1	0.009(1)
M8	0.0511(1)	0	0.1548(1)	1	0.009(1)
M9	0.4071(1)	0.1779(1)	0.0860(1)	1	0.010(1)
M10	0.4517(1)	0	0.0365(1)	1	0.010(1)
M11	0.5996(1)	0.3221(1)	0.1038(1)	1	0.010(1)
M12	0.1095(1)	0.1792(1)	0.2077(1)	1	0.012(1)
M13	0.9598(1)	0	0.2290(1)	1	0.013(1)
M14	0.7388(1)	0.8726(1)	0.0923(1)	1	0.015(1)
M15	0.1201(1)	0.6850(1)	0.0236(1)	1	0.017(1)
M16	0.8720(1)	0.8115(1)	0.1583(1)	1	0.012(1)
M17	0.7194(1)	0.1233(1)	0.2208(1)	1	0.012(1)
M18	0.9667(1)	0	0.0781(1)	1	0.011(1)
M19	0.2031(1)	0.1169(1)	0.0331(1)	1	0.013(1)
M20	0.3038(1)	0.1103(1)	0.1552(1)	1	0.010(1)
M21	0.5251(1)	0	0.1142(1)	1	0.011(1)
M22	0.5146(1)	0	0.1927(1)	1	0.012(1)
M23	0	0	0	1	0.013(1)

[a] Structure refined with M1–M6: Pd and M7–M23: Cd.

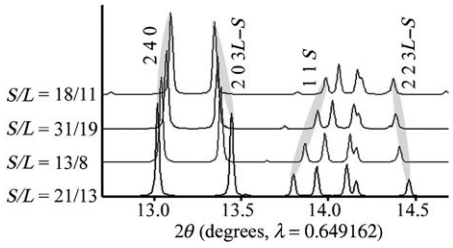

Figure 1. A region of four theoretical powder patterns calculated for the $Pd_{20.4}Cd_{79.6}$ ($S/L = 18/11$), $Pd_{21.1}Cd_{78.9}$ ($S/L = 31/19$), $Pd_{0.213}Cd_{0.787}$ ($S/L = 13/8$), and $Pd_{0.235}Cd_{0.765}$ ($S/L = 21/13$) structures ($\lambda = 0.649162$ Å). The grey ellipses indicate peaks with related *hkl* indices, *l* being a function of *S* and *L*. For example, the $203L-S$ peak for $S/L = 18{:}11$ is 2015 ($15 = 3L-S = 3\times11-18$).

Table 4. Peaks in the $Pd_{0.213}Cd_{0.787}$ synchrotron[a] powder pattern with unique *hkl* assignment.

hkl	$2\theta_{obs}$	2θ range[b]
240	12.978	12.958–13.026
$203L-S$	13.322	13.223–13.429
$11S$	13.813	13.784–13.859
$022L$	16.905	16.847–16.953
$243L-S$	17.044	16.954–17.135
$31S$	17.436	17.048–17.476
$222L$	18.508	18.441–18.548
$263L-S$	20.811	20.703–20.871
$134L-S$	21.031	20.863–21.140
$604L-S$	23.368	23.252–23.407
$154L-S$	23.601	23.420–23.682

[a] $\lambda = 0.649162$ Å. [b] See master list (Supporting Information).

As a final test, for those models for which we had a single-crystal structure, we directly compared the full theoretical and experimental patterns. Two such full comparisons are given in the Supporting Information.

For the sake of completeness, the structural refinements of $Pd_{0.213}Cd_{0.787}$ and $Pd_{0.235}Cd_{0.765}$ as (3+1)-dimensional crystals using the Jana2000 suite of programs.[39] are given in the Supporting Information. The models for $Pd_{0.213}Cd_{0.787}$ and $Pd_{0.235}Cd_{0.765}$ were quantitatively and semi-quantitatively, respectively, similar: the same atom sites were uncovered with the same occupation factors (see Supporting Information). As there was no particular advantage to either ordinary three-dimensional or (3+1)-dimensional refinement, the data reported in the text is given in the format most readily understandable by the larger number of chemists, that is, that of ordinary three-dimensional crystals. Finally, it proved impossible, with the software available, for our group to refine the (3+1)-dimensional synchrotron powder data. Our current program allows for only a uniform peak profile while synchrotron radiation peak profiles are variable as a function of peak position.[40]

Finally, more traditional three-dimensional least-squares powder refinement based on room temperature synchrotron powder data for both the $Pd_{0.213}Cd_{0.787}$ and $Pd_{0.235}Cd_{0.765}$ phases is included in the Supporting Information.

Electronic structure calculations: Electronic structure calculations were used in conjunction with single-crystal X-ray data to derive Cd versus Pd site preferences. The electronic structure method for determining Pd–Cd site occupancies has three steps. First we carried out LDA-DFT calculations on the parent structure of the family, γ-brass.[37,41,42] We then found

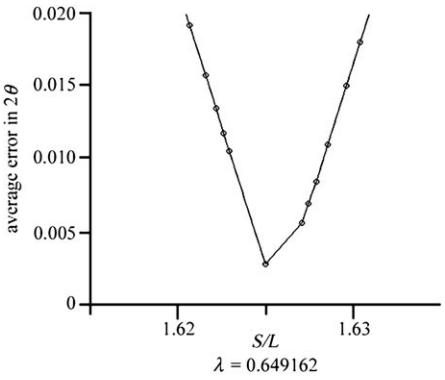

Figure 2. The average error in 2θ associated with linear least-squares fits of the $Pd_{0.213}Cd_{0.787}$ synchrotron powder pattern. The experimentally observed peaks were indexed for *hkl* peaks assuming *l* is a function of *S* and *L*. Open circles represent the calculated points (all *S*/*L* ratios between 1.62 and 1.635 with *S* and *L* integers for *S* no greater than 100). The minimum value at $S/L = 1.625$ corresponds to $S/L = 13{:}8$. These are the *S* and *L* values observed in the $Pd_{0.213}Cd_{0.787}$ single-crystal structure.

extended Hückel (eH) parameters that reproduced the band structure of the LDA-DFT calculation. We then used the standard molecular orbital approach, calculating the Mulliken charge populations on a hypothetical model, to assign Cd versus Pd site preferences.[43–46] In this hypothetical model the atomic coordinates of the $Pd_{0.213}Cd_{0.787}$ and $Pd_{0.235}Cd_{0.765}$ structures were taken, but the same generic Cd parameters were used for all atomic sites. We assumed that the more electronegative Pd atoms preferentially occupy the sites with the highest Mulliken populations, that is, those that have the most electrons. This assumption has proven reliable in many instances of site orderings in intermetallic compounds.[43–46] Accordingly, we placed Pd atoms at the more electron-rich sites and Cd at the less electron-rich sites, see the Results section below.

LDA-DFT calculations were carried out on the cubic γ-brass structure by using the VASP package.[47–50] There is one Pd–Cd cubic γ-brass structure in the literature, but it contains partial occupancies that are difficult to model with electronic structure calculations, so we performed our calculations on an idealized γ-brass model in the space group $I\bar{4}3m$. Following the site preferences observed in the Pd_8Cd_{43} structure,[51] we placed Pd atoms at the OT positions, and Cd atoms at the remaining positions. From this initial structural model, the generation of a band structure for this system involved a sequence of calculations. Optimizations of first the volume, and then the atomic positions, were carried out using a $3\times3\times3$ *k*-point mesh. The charge density and the potential were then calculated by using a $5\times5\times5$ *k*-point mesh (both meshes generated with the Monkhorst–Pack scheme).[52] Using this charge density and potential, the band structure shown in Figure 3a was then calculated *k*-point by *k*-point. Ultra-soft Vanderbilt pseudopotentials[53] were used throughout. Plane wave basis sets were used in the low-precision mode. This corresponded to an energy cut-off of 149.2 eV.

We then sought generalized eH parameters that reproduced the features of this LDA-DFT band structure. We carried out calculations on the cubic γ-brass using the YAeHMOP package.[54] As our later calculations on the $Pd_{0.213}Cd_{0.787}$ and $Pd_{0.235}Cd_{0.765}$ structure were to be performed using the experimental cell parameters, rather than LDA-DFT optimized geometries, we calibrated the eH parameters using an idealized γ-brass structures with average experimental distances taken from each site type of the Pd_8Cd_{43} structure[51] and atomic Mulliken populations were obtained from averaging over a $15\times15\times15$ Monkhorst Pack *k*-point mesh,[52] using the same eH parameters for all atoms. The default Cd parameters[55] proved reasonable, as can be seen by comparison of Figure 3b with the LDA-DFT calculation of Figure 3a. While there were some differences between this band structure and that calculated at the LDA-DFT level, the overall features near the Fermi energy matched. These

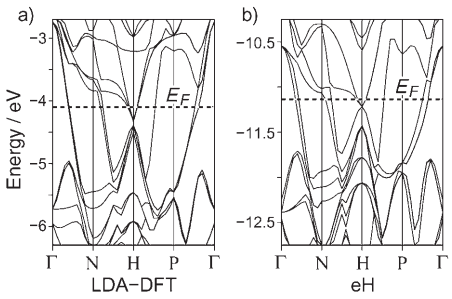

Figure 3. Band structures of the Pd/Cd cubic γ-brass structures near the Fermi energy calculated with a) the LDA-DFT (Pd_2Cd_{11}) and b) extended Hückel (eH) methods. The eH calculation was performed using generic Cd-based parameters (see text). High symmetry *k*-points are for the reciprocal lattice of the primitive γ-brass unit cell:[115] N for $k=(0,0,0.5)$, H for $k=(0.5,-0.5,0.5)$, and P for $k=(0.25,0.25,0.25)$.

parameters were: H_{ii}(Cd 5s) = −11.8 eV, $\zeta_s = 1.64$; H_{ii}(Cd 5p) = −8.2 eV, $\zeta_p = 1.60$.

The electronic structures of both orthorhombic systems, $Pd_{0.213}Cd_{0.787}$ and $Pd_{0.235}Cd_{0.765}$, were then calculated at the eH level, again using Cd parameters at all sites. For structures $Pd_{0.213}Cd_{0.787}$ and $Pd_{0.235}Cd_{0.765}$ atomic Mulliken populations were averaged from 32 *k*-points distributed evenly across the $(+k_x, \pm k_y, \pm k_z)$ half of the first Brillouin Zone.

Results

Overall structural family

Preliminary description of the $Pd_{0.213}Cd_{0.787}$ and $Pd_{0.235}Cd_{0.765}$ structures: We report in this paper two single-crystal structures in the $Pd_{1-x}Cd_x$ system situated next to the γ-phase field. Since these crystal structures are closely related to the γ-brass structure type (Cu_5Zn_8), it is helpful to review the structure of γ-brass itself. The γ-brass structure type is often viewed as a series of concentric polyhedra[56] as shown in Figure 4 (it can be described in other ways[57]). Each of the four inequivalent sites of the structure form separate polyhedra: inner tetrahedron (IT), outer tetrahedron (OT), octahedron (OH), or cuboctahedron (CO). While this description is visually striking and has great value due to its simplicity and ease of description, it obfuscates another geometrical feature of great relevance to the newly uncovered phases.

We show in Figure 5 the coordination environments for each of the four sites. The IT, OT, OH, and CO sites lie in the center of an icosahedron, icosahedron, closo-11 deltahedron, and an irregular 11-coordinate polyhedra, respectively. The icosahedron around the OT site shares an edge with a closo-11 deltahedron and these pairs of polyhedra form chains of linked polyhedra (shown in Figure 6a, running along the $[\bar{1}10]$ direction). These chains have a mirror plane bisecting them, normal to the [110] direction. Of particular interest are the atoms that lie in this mirror plane itself: these atoms are given at the bottom of Figure 6a. As this figure shows, the atoms in this central plane can be decomposed into two sets, one in blue and the second in green.

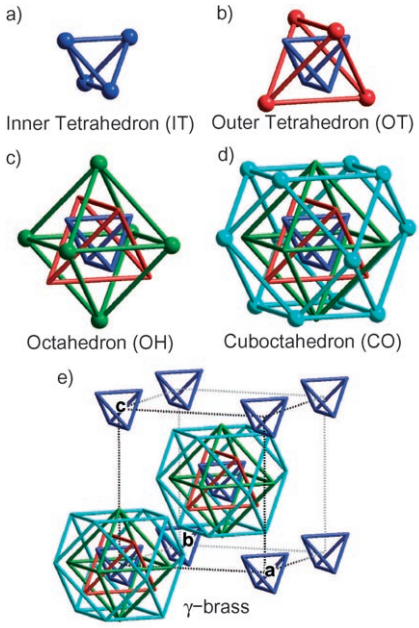

Figure 4. The cubic γ-brass (Cu_5Zn_8) structure, viewed in terms of the polyhedra formed by each of its four symmetry-distinct sides: a) the inner tetrahedron (IT), blue; b) the outer tetrahedron (OT), red; c) the octahedron (OH), green; and d) the cuboctahedron (CO), light blue. Together they form a 26-atom cluster. e) The cubic γ-brass structure consists of a bcc packing of these clusters.

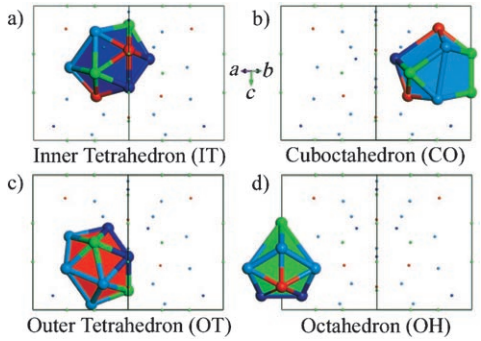

Figure 5. The coordination environments around the four sites of Cu_5Zn_8 (γ-brass). IT: dark blue, CO: light blue, OT: red, OH: green. The coordination polyhedra of a) the IT site, a distorted icosahedron; b) the CO site, an irregular 11-coordinate polyhedron; c) the OT site, a distorted icosahedron; and d) the OH site, a closo-11 deltahedron.

These two sets of atoms have different periodicities in the [$\bar{1}$10] direction, the blue atoms forming a chain with $L=3$ atoms per unit cell, and the green atoms forming a chain with $S=5$ atoms per unit cell. In the γ-brass structure type the L and S distances are in the ratio $1.67=5{:}3$.

The structures reported here ($Pd_{0.213}Cd_{0.787}$ and $Pd_{0.235}Cd_{0.765}$) are also shown in Figure 6, in which it can be seen that they are closely related to Cu_5Zn_8. They can also be described as vertex sharing chains of icosahedra and closo-11 deltahedra, and furthermore can also be described in terms of S and L chains of atoms. The difference between the $Pd_{0.213}Cd_{0.787}$ and $Pd_{0.235}Cd_{0.765}$ structures and γ-brass itself are that the first two structures are orthorhombic rather than cubic, that their chains run in the orthorhombic [001] direction rather than the cubic [$\bar{1}$10] direction, and that the ratio of L and S distances are 13:8 and 21:13, respectively, rather than 5:3. We further note that the L and S values for the three structures are all between neighboring members of the Fibonacci sequence: 1, 2, 3, 5, 8, 13, 21.. . We observe that the S/L ratios hover near the golden mean ($\tau=(1+\sqrt{5})/2\approx1.618$), a number that is the asymptotic value for ratios of consecutive Fibonacci numbers.[12,58,59]

S/L as a function of x, *$Pd_{1-x}Cd_x$, $0.755\geq x\geq0.800$*: The previous section gives a description of the $Pd_{0.213}Cd_{0.787}$ and $Pd_{0.235}Cd_{0.765}$ structures. We now place these phases in the context of other Pd:Cd composition ratios. In this section we report results based on powder data for $Pd_{1-x}Cd_x$, $0.755\geq x\geq0.800$ samples. Powder patterns for samples with such compositions were indexed following the scheme given in the Experimental Section. The resulting best fit S/L values are shown in Figure 7, which shows the S/L ratios of the two structures for which we have fully resolved single-crystal structures.

As can be seen in this figure, the two single-crystal S/L ratios are fully subsumed in a larger range of S/L values. (error bars given in Figure 7 correspond to those S/L values in which average 2θ error is $\leq0.005°$). S/L values extend from $S/L=21/13$ (1.615) to near 1.64. The lower limit is within experimental error of the golden mean.

We therefore expect that it will prove possible to find crystal structures with other S/L values. However, the data so far is insufficient to determine whether the S/L ratio varies continuously as a function of x, or whether there are certain preferred values. As the former would correspond to incommensurate and the latter commensurate structures, we can not as yet determine whether these phases are commensurate or incommensurate.

In Figure 8, by the same procedure, the refined a and b axis lengths are shown. As can be seen there is a steady increase in cell axes with increasing Cd content. Such a result is compatible with the metallic radii of the two elements (for Pd and Cd they are 138 and 149 pm, respectively). These results substantiate the phase evolution in the studied stoichiometric range.

We have examined other x values (for $Pd_{1-x}Cd_x$) as well. For x greater than 80 mole percent, even with synchrotron radiation, it proves not possible to find enough unique reflections to unambiguously determine the cell parameters. Indeed powder patterns for $Pd_{18.0}Cd_{82.0}$ are indexed as cubic (the Cu_5Zn_8 structure type). Complications also appear for x less than 75.5 mole percent. For example, with $Pd_{25.0}Cd_{75.0}$, new and strong extra peaks appear, presumably due to a different structure variant from the structures reported in this paper.

These data suggest that the two existing structures exist as two possibilities among a number of other structures; for $Pd_{1-x}Cd_x$, $0.755\geq x\geq0.800$ they are related to one another by different S/L ratios. In the remainder of this paper we

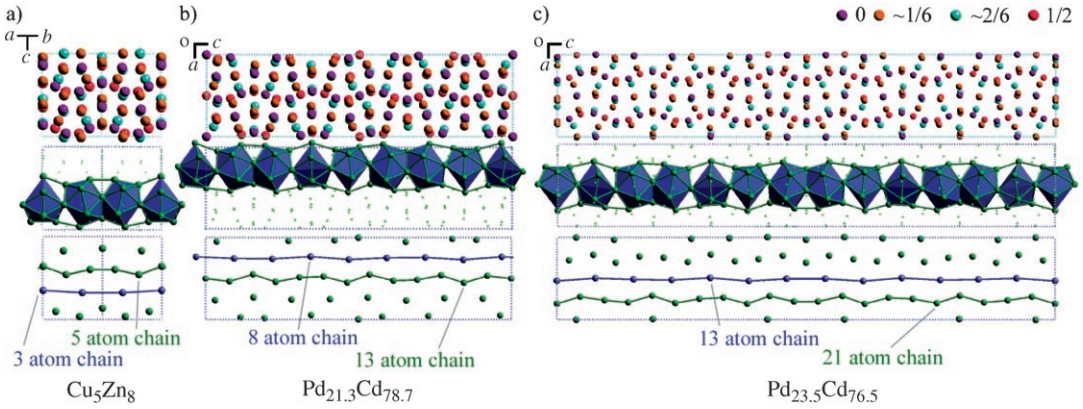

Figure 6. The structures of $Pd_{0.213}Cd_{0.787}$ and $Pd_{0.235}Cd_{0.765}$. a) The cubic γ-brass (Cu_5Zn_8) structure. b) The $Pd_{0.213}Cd_{0.787}$ structure. c) The $Pd_{0.235}Cd_{0.765}$ structure. Top panels: views down the b axis ($a+b$ for Cu_5Zn_8). Heights are indicated with color: purple atoms at height $b=0$, orange at 1/6, light blue at 2/6, red at 1/2. Middle panels: chains of vertex sharing closo-11 deltahedra and icosahedra occurring in these structures (vertices in green and centering atoms in blue) centered at height $b=1/2$. Bottom panels: chains in the $b=1/2$ layer of atoms (vertex atoms of the above polyhedra still shown in green, centering atoms in blue).

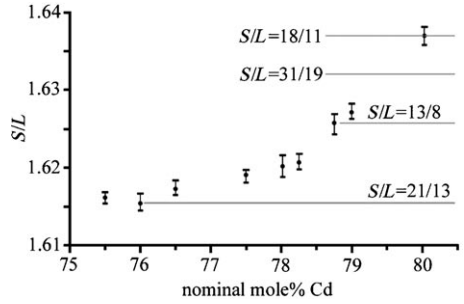

Figure 7. The S/L versus mole % Cd for $Pd_{1-x}Cd_x$ ($.755 \le x \le .800$) samples (from synchrotron powder patterns). Filled dots: S/L values with best fit to the powder data. Error bars: range in which S/L values have an average error in $2\theta \le 0.005$. For convenience, the S/L values for the $Pd_{0.213}Cd_{0.787}$ and $Pd_{0.235}Cd_{0.765}$ structures are given.

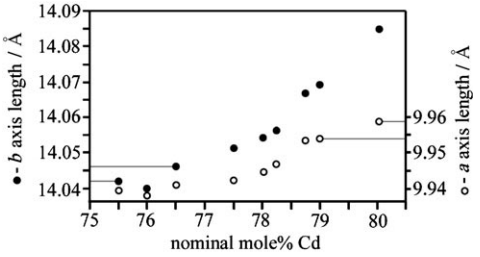

Figure 8. Best fit a and b cell parameters (from synchrotron powder patterns) versus mol % Cd for $Pd_{1-x}Cd_x$ ($.755 \le x \le .800$) samples. Closed circles: a axis lengths. Open circles: b axis lengths.

will further define shared characteristics of these phases. As our structural analysis will suggest, the origin of the varying structures lies in the presence of chemical twinning interfaces and that these interfaces are related to changes in Pd versus Cd ratios. We therefore turn first to the issue of Cd versus Pd sites in the single-crystal structures.

Cd and Pd site preferences: As we shall see, the Cd versus Pd sites in the observed crystals play a significant role in our understanding of the structures. Unfortunately, as our structural data is ordinary X-ray data and furthermore as Pd and Cd are nearly adjacent elements on the periodic table, it is difficult to determine site preferences directly from the structural data. Nevertheless, we shall see that the exhaustive combination of both X-ray data in conjunction with electronic structure calculation, will provide us with a firm model as to the Cd versus Pd site preferences in these systems.

We begin with the $Pd_{0.213}Cd_{0.787}$ system. The structural model (see Table 1 and Table 3) contains 276 atoms in the unit cell divided into twelve general 16g, ten special 8f, and one special 4a sites. The nominal $Pd_{0.213}Cd_{0.787}$ composition and the measured microprobe composition of $Pd_{21.61(3)}Cd_{78.39(3)}$ allow six of the atom positions to be occupied by Pd atoms. This figure corresponds to two 16g and three 8f sites fully occupied by Pd atoms and one 8f site roughly 40 % occupied by Pd atoms. (We could of course substitute two more 8f sites for any one 16g without changing the total occupation).

We therefore considered the 26820 alternatives in which three 16g and two 8f sites (or alternatively four, two, one or zero 16g and zero, four, six or eight 8f sites, respectively) were occupied by Pd atoms, all other positions being taken by Cd atoms. We determined the R_1 factor for all of these possibilities (after allowing each model to be structurally refined in the SHELX program).[60] R_1 factors ranged from 2.6–3.6 %, a range which spans roughly 25 % of the total R_1 factor.

These results are shown in histogram form in Figure 9. The histogram has the shape of a bell curve with a tail running to low R_1 factor values. The inset at the upper left corner shows an enlargement of this tail. We can see that the structure with the lowest R_1 factor lies below the continuum of the other R_1 factors. The lowest R_1 factor structure is therefore of particular interest: in this structure the M1–M6 sites are occupied by Pd atoms while the M7–M23 positions are occupied by Cd.

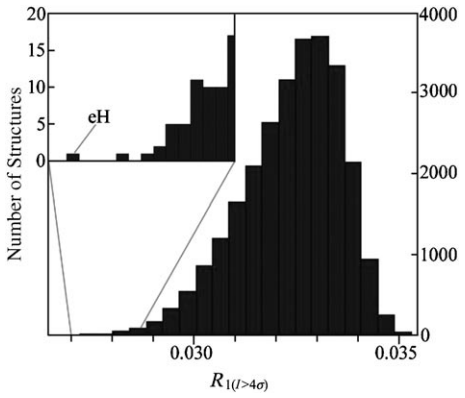

Figure 9. Histogram plotting the $R_{1(I>4\sigma)}$ values for the 26820 possible ordering patterns of the $Pd_{0.213}Cd_{0.787}$ structure with a composition of 64 Pd and 212 Cd atoms per unit cell. The lowest R_1 value (2.72%, default SHELX-l97 weighting scale, see inset) corresponds with the site-ordering pattern suggested by extended Hückel (eH) calculations (see text).

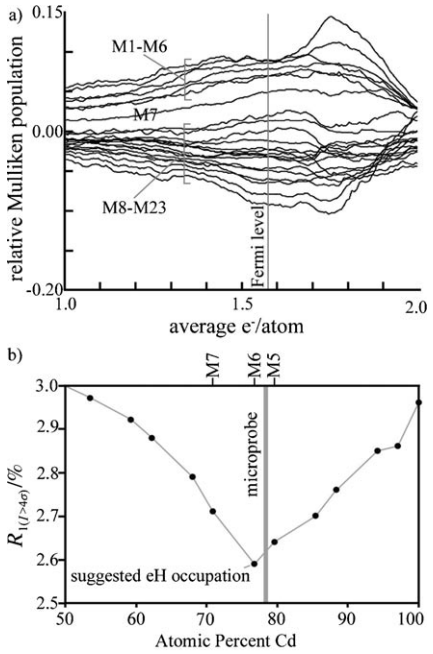

Figure 10. a) The relative Mulliken population versus average valence electrons per atom for the $Pd_{0.213}Cd_{0.787}$ structure. Sites are numbered in order of decreasing relative Mulliken population. Three groups of sites can be discerned: M1 M6 are electron rich, M7 is intermediate, and M8–23 are electron poor. b) The refined $R_{1(I>4\sigma)}$ values for a sequence of decreasing Pd occupation: M7 is for only M1 M7 Pd, M6 only M1 M6 Pd and so forth. The lowest $R_{1(I>4\sigma)}$ value is for M1 M6 Pd, the electron-rich set of sites in a). Grey bar: microprobe composition (with a $\pm 3\sigma$ error margin) of the $Pd_{0.213}Cd_{0.787}$ single crystal.

We now compare these X-ray structural results with predictions based on electronic structure calculations. The electronic structure calculations used are extended Hückel (eH) calculations in which the electronic structure parameters are chosen to match output at the LDA-DFT level (see Experimental Section). Such LDA-DFT optimized eH calculations have proven quite reliable in our hands.[61–63] Furthermore, it is well established that eH calculations are useful in predicting site preferences.[43–46]

As described in the Experimental Section, the eH method of determining site preferences requires calculation of the Mulliken charge population of an average structure in which a generic metal atom is placed at all metal sites. Guided by experiment, those sites with a greater electron density (i.e., have a higher Mulliken population) are taken to be Pd sites; conversely, those sites that are more electron deficient are made into Cd positions. This atomic ordering is in agreement with the Pauling electronegativity of the two elements which are 2.20 and 1.69, respectively (other electronegativity scales it should be noted place these two elements differently).[64]

The Mulliken population analysis for $S/L = 13/8$, the $Pd_{0.213}Cd_{0.787}$ structure, is shown in Figure 10a. Here, we plot the relative Mulliken populations (the deviation from the average electron count) of each site as a function of the average electron concentration. The sites fall roughly into three groups: sites M1–M6 form a group at high electron counts (between about 0.03 and 0.08 excess electrons per atom), M7 at intermediate electron counts, and the sites M8–M23 at low electron counts (they form a bundle centered around −0.03 electrons per atom).

We see that the experimental results based on *R* factors and the theoretical result based on LDA-DFT optimized eH theory give exactly the same result: sites M1–M6 are occupied by the more electron-rich Pd, while M7–M23 are occupied by the more electron-poor Cd. Indeed, as the relative Mulliken populations appear to be of use, we have ordered all 23 sites by their relative Mulliken population. Thus M23, located on the special 4a site is the most electron-poor site of all.

Full Pd occupation of the M1–M6 sites corresponds to 64 Pd atoms in the unit cell, a number in general agreement with the microprobe result of 60 ± 1 Pd atoms (though, of course, partial occupancy of sites can not be excluded). We may use the X-ray data in conjunction with the quantum calculations to test the overall notion that only six of the sites are primarily occupied by Pd atoms. To do so we directly compare the *R* factor for which no atoms are assumed to be Pd atoms (i.e., all atoms are assumed to be Cd atoms), for which only M1 is assumed to be Pd, for which M1, M2 are assumed to be Pd, and so forth.

The results of these calculations are shown graphically in Figure 10b. Note the *R* factors given are after SHELX refinement. As this figure shows, the *R* factors form roughly a "V" shape, with the minimum of the "V" located at sites M1–M6 occupied by Pd atoms. The number of Pd atoms from the single-crystal data set is in reasonable agreement with microprobe findings and the nominal composition (59 Pd atoms). Furthermore, as we mentioned in the Experimental Section, not only does the single-crystal structure correspond to the refined powder pattern *S*/*L* values, but also no other phase is observed in the synchrotron powder data. All data appear in accord.

This proposed site-preference model, based on the concordance of ordinary single-crystal X-ray diffraction data and tight-binding quantum calculations, can be further tested through more rigorous diffraction methods including neutron and resonant dispersion synchrotron diffraction, with the latter method more easy to apply in the current situation.

We now turn to the $Pd_{0.235}Cd_{0.765}$ system. The orthorhombic unit cell contains 448 atoms per unit cell distributed over 39 different sites. This is significantly more than in the previous system. While before, it was possible to directly evaluate the *R* factor for different Pd occupation patterns, we are no longer able to apply such a direct procedure. Just considering those occupations that have a total occupation near the value determined by microprobe would require refinement of 10^8 possibilities, a number which on our computer systems would require on the order of ten years.

Instead we use quantum calculations to guide the choice of systems refined. In Figure 11a we show the relative eH Mulliken populations of the $Pd_{0.235}Cd_{0.765}$ system. As before,

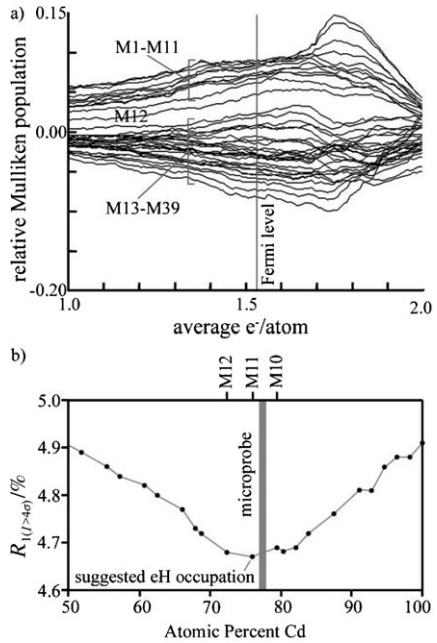

Figure 11. a) The relative Mulliken population versus average valence electrons per atom for the $Pd_{0.235}Cd_{0.765}$ structure. b) The refined $R_{1(I>4\sigma)}$ values versus Pd–Cd composition. See caption to Figure 10 for abscissa axis definition. For a), as in the $Pd_{0.235}Cd_{0.765}$ structure (Figure 10a), the relative Mulliken populations divide the sites into three groups: M1–M11: electron rich, M12: intermediate, and M13–39: electron poor. The lowest $R_{1(I>4\sigma)}$ value occurs for M1–M11 Pd and M12–M39 Cd.

the relative Mulliken populations cluster into three groups: M1–M11 being electron rich, M12 being intermediate, and M13–M39 being electron poor. (Again the number of the site refers to the relative order of the Fermi level Mulliken population).

In Figure 11b, we compare the single-crystal refinement *R* factors for Pd–Cd occupancy models for sequential occupation of the various M sites. Thus we compare the *R* factor for which all atoms are assumed to be Cd atoms, for which only M1 is a Pd atom, for which only M1 and M2 are Pd atoms, and so forth. The resultant *R*-factor appears somewhat parabolic in shape. The minimum of this *R* factor is for M1–M11 as Pd, a value very near the measured microprobe composition of the sample (see figure).

One difference between the $Pd_{0.235}Cd_{0.765}$ and $Pd_{0.213}Cd_{0.787}$ samples is in the sharpness of their curves. The former curve is "V"-shaped, the latter more parabolic. We can think of two possible explanations for the more parabolic shape. First, it is possible that for $Pd_{0.235}Cd_{0.765}$ there is a greater degree of mixed Cd and Pd sites (say for M9–M12). Second, and perhaps more to the point, the X-ray data for the $Pd_{0.235}Cd_{0.765}$ crystal is worse than the data for $Pd_{0.213}Cd_{0.787}$. Compare for example their respective *R* factors: 4.7 versus 2.6% or the number of measured reflections, see Table 1. The $Pd_{0.235}Cd_{0.765}$ structure is simply murkier than for $Pd_{0.213}Cd_{0.787}$. However, for simplicity in the next section, for the $Pd_{0.235}Cd_{0.765}$ structure, we will call M1–M11 Pd sites and M12–M39 Cd sites. This nomenclature should be understood in light of the above statements.

Discussion

A Laves phase view of γ-brass, $Pd_{0.213}Cd_{0.787}$, and $Pd_{0.235}Cd_{0.765}$: In the previous section, we saw that eH Mulliken population calculations were useful in determining the Pd–Cd site orderings. In this section, we shall see that these same Mulliken populations will lead to a more revealing view not just of $Pd_{0.213}Cd_{0.787}$ and $Pd_{0.235}Cd_{0.765}$, but of the γ-brass structure itself. We will find that the γ-brass, $Pd_{0.213}Cd_{0.787}$ and $Pd_{0.235}Cd_{0.765}$ structures all consist of fragments of the widespread intermetallic cubic Laves phase structure, the $MgCu_2$ type.

We begin with γ-brass. We consider the four crystallographically inequivalent sites: IT, OT, OH and CO, not following the classical view as polyhedra, but instead through the prism of their Mulliken populations. This view is shown in Figure 12. Here, the Mulliken populations of each site are plotted as a sphere: the color of the site's sphere reflects whether the site is more negatively charged (white) or less negatively charged (black) with respect to the mean electron charge per atom. The volume of the sphere is proportional to how electron poor or rich the site is. In Figure 12b,c, the electron-poor and -rich sites are drawn separately: OT and OH sites are electron poor, while IT and CO sites are electron rich.

When tracing out the networks of the electron-poor (blue) and electron-rich (red) atoms separately, familiar patterns arise. The OT and OH sites together form an adamantane-shaped cluster (Figure 12b), while the IT and CO sites form as one central tetrahedron, each corner of which is vertex sharing to another tetrahedron, forming a tetrahedron of tetrahedra (TOT). Both clusters have T_d symmetry. These clusters are known in intermetallic chemistry. They

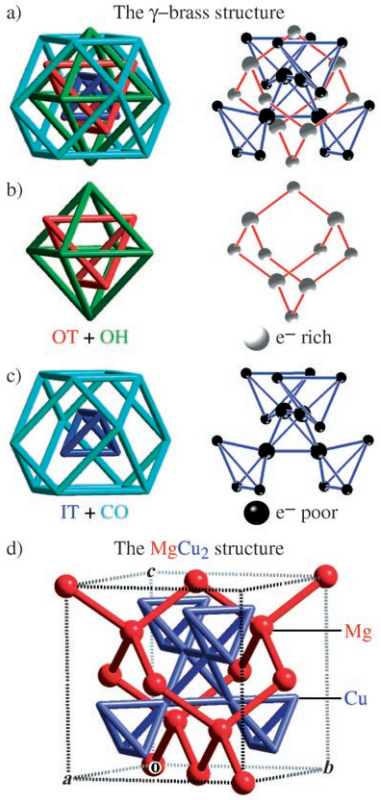

Figure 12. a) Two views of the γ-brass structure. Left: traditional polyhedra view. Right: a view derived from observed site preferences and confirmed with Mulliken population calculations: the relative Mulliken population of each atom is plotted as spheres. Sphere volumes: extent of excess charge. Sphere color: sign of excess charge (white: negative, black: positive). b) The connections within the electron-rich set of sites creates an adamantane cage. c) The connections between the electron-poor sites trace out a tetrahedron of vertex-sharing tetrahedra (TOT). d) The adamantane cage and tetrahedron of tetrahedra both occur in the $MgCu_2$ structure type.

are found in the widely occurring $MgCu_2$ structure type (Figure 12d).[65–67] In the $MgCu_2$ structure, the clusters form part of larger networks: the adamantane cluster continues unimpaired to become part of an extended diamond network, while the TOT extends onward to form a network of vertex-sharing tetrahedra (a diamondlike network in which each atom site of diamond is replaced by a vertex-sharing tetrahedron).

By contrast, in the γ-brass structure, the diamond and vertex-sharing tetrahedral networks are truncated down to form a single adamantane cage and a single tetrahedron of tetrahedra. Together these comprise the 26-atom $MgCu_2$-type fragments shown in Figure 12a–c. In γ-brass we find a body-centered cubic arrangement of these 26-atom clusters.

The relative Mulliken populations of the four sites are in the order: IT, CO, OH, and OT. These are in accord with the experimentally observed site preferences of known binary γ-brass structures. A short list of such systems is shown in Table 5. In this table we give the distribution of the two elements of each site over the four γ-brass sites. As

Table 5. Selected observed site ordering for γ-brass type structures.[a]

Compound	IT	CO	OH	OT
Ag_5Zn_8[116]	1 Zn	1 Zn	1 Ag	1 Ag
Ag_2Hg_3[117,118]	1 Hg	0.92 Hg	1 Ag	1 Ag
Pd_8Cd_{43}[51]	1 Cd	1 Cd	1 Cd	1 Pd
$PtCd_5$[51]	0.5 Cd	1 Cd	1 Cd	1 Pt
Al_4Cu_9[97,102,119]	0.5 Al/0.5 Cu	0.5 Al/0.5 Cu	1 Cu	1 Cu
Cu_5Cd_8[94,97]	1 Cu	0.1 Cu/0.9 Cd	0.3 Cu/0.7 Cd	1 Cu

[a] Structures are selected for those in which site preferences have been determined and for which electron counts lie within 0.1 electron per atom of the Hume-Rothery rule 21:13 (i.e., near the golden mean), and are not high-temperature phases. A more complete list is given in the Supporting Information.

expected from the Mulliken populations, one atom type tends to occupy the first IT site followed by the CO and sometimes the OH sites, while the other atom type occupies first the OT and then the OH sites. The sole exception of which we know is Cu_5Cd_8, the last entry in the table.

We now use these same principles to view the $Pd_{0.213}Cd_{0.787}$ and $Pd_{0.235}Cd_{0.765}$ structures. We directly calculate the Mulliken population of the various sites and then connect sites of similar charge. Again we are looking for $MgCu_2$-like pieces. The resulting picture is shown in Figure 13. (Similar results are found for the $Pd_{0.235}Cd_{0.765}$ structure). Two types of fragments occur. One is the 26-atom cluster found in the γ-brass structure itself. These occur in paired layers along the *c* axis. Separating these paired layers is a second type of cluster, which we term the interface cluster. It is a smaller fragment of the $MgCu_2$

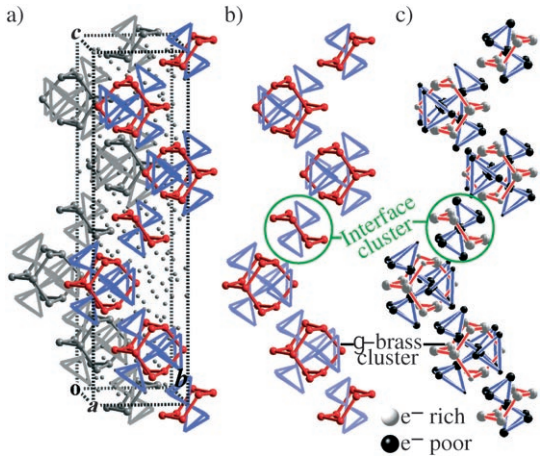

Figure 13. $MgCu_2$-type clusters in the $Cd_{0.213}Pd_{0.787}$ structure. a,b) The sequence of $MgCu_2$-type clusters along the *a* axis, a) drawn in the unit cell, b) drawn separately. b) Pairs of γ-brass polyhedra (each with an adamantane cage in red, and a tetrahedron of tetrahedra (TOT) in blue), separated by smaller interface clusters (one of which is circled in green). In the interface clusters, the adamantane cage and TOT have been truncated to respectively a six-membered ring in the chair conformation (red), and a pair of vertex-sharing tetrahedra (blue). c) These clusters viewed with their Mulliken populations (see caption of Figure 12 for details). Adamantane (and chair) sites are electron rich, while the vertex-sharing tetrahedra sites are electron poor.

structure: it consists of a single six-membered ring chair and a pair of vertex-sharing tetrahedra.[68]

The Laves derived picture of γ-brass is thus of real use in understanding the more complex $Pd_{0.213}Cd_{0.787}$ and $Pd_{0.235}Cd_{0.765}$ structures. In these systems as well as the simpler γ-brass structure, clusters which are $MgCu_2$-like form core building blocks. Furthermore these building blocks are fundamentally connected to the Pd–Cd makeup of the individual systems. Pd atoms appear to be exclusively located at adamantane and chair positions, while Cd atoms are located on vertex-sharing tetrahedra. In the next section, we shall see how the 13-atom clusters can be derived from the 26-atom clusters, and in so doing we will generate a principle by which both $Pd_{0.213}Cd_{0.787}$ and $Pd_{0.235}Cd_{0.765}$ can be derived from γ-brass.

Twinning law derived from γ-brass itself: The last section showed that the $Pd_{1-x}Cd_x$, $0.755 \geq x \geq 0.800$ phases are built up from clusters of the simpler Laves phases. Principal clusters are 26-atom $MgCu_2$-like pieces; interface clusters are 13-atom $MgCu_2$-like pieces. The interface clusters lie at interfaces of domains of the principal clusters. This general picture is a familiar one in solid-state chemistry. Such domains are described as inversion domains and the interfaces described as being due to chemical twinning.[61,69–78] In this section we explore in depth the twinning law present in these phases. We will see that this twinning principle is directly derived from the γ-brass structure itself.

In Figure 14a, we show that γ-brass is a body-centered crystal built up from the 26-atom principal cluster: the adamantane portions of the structure are given as balls-and-sticks; the tetrahedron of tetrahedra as sticks alone. The former cluster is comprised of OT and OH atoms, the latter of IT and CO atoms. Of great pertinence to the twinning law is an alternate set of adamantane and tetrahedron of tetrahedra networks. This alternate set, shown in Figure 14b, is seen here in γ-brass itself.

In the alternate view, the two-coordinate OH sites (of the adamantane cluster) are half replaced by CO sites. The sites forming the tetrahedron of tetrahedra have also changed: the central tetrahedron is now comprised of three CO and only one IT site; three of the twelve outer tetrahedral sites are now occupied by OH atoms. As Figure 14 shows, these new clusters are shifted in the $a+b+c$ direction with respect to the original clusters. Moreover they are inverted in orientation. The bond angles in the new cluster are also less perfect. Note, for example, the flattened CO-OT-CO bond angle in the new adamantane pieces.

In Figure 15 these two clusters are juxtaposed one on top of the other. At the top of this figure the union of the two clusters is shown, on the bottom their intersection (shown in purple). The intersection is composed of a single chair and two vertex-sharing tetrahedra. This cluster is the same 13-atom cluster that we have previously termed as the interface cluster. In both parts of Figure 15 a pseudo C_2 axis can be seen passing through the two parts.

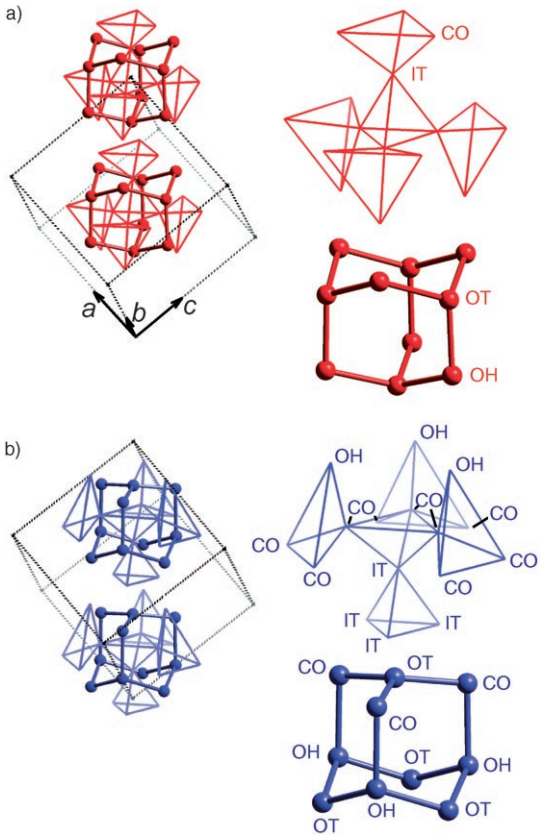

Figure 14. The standard and alternate $MgCu_2$-type fragments in the cubic γ-brass structure. a) The standard fragments with the adamantane cage formed from OH and OT sites, and the tetrahedron of tetrahedra (TOT) from IT and CO sites. b) Alternate $MgCu_2$-type fragments generated by drawing a different set of connections. For alternate connections, the adamantane cage is built not only from OH and OT sites, but also CO sites; the tetrahedron of tetrahedra consists of IT, CO, and OH sites. Note that the standard and alternate $MgCu_2$-type fragments are of inverted orientation with respect to each other.

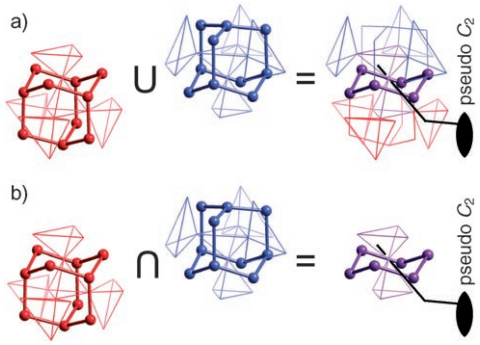

Figure 15. Juxtaposition of the standard and alternate $MgCu_2$-type fragments in the cubic γ-brass structure shown in Figure 14. a) The union and b) intersection of the standard (red) and alternate (blue) fragments. The intersecting region between the two fragments is shown in purple.

With these notions in hand, we can discuss a twinning principle present in γ-brass. In Figure 16 we show a portion of γ-brass in which the two cluster representations are both present, related to one another by the pseudo C_2 axis. The

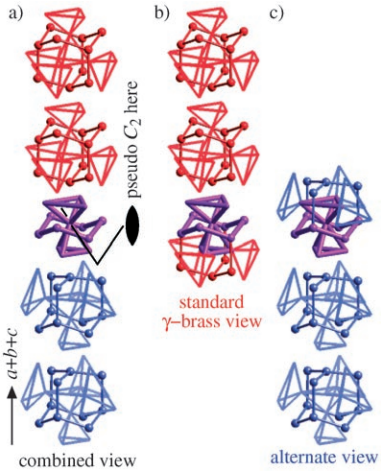

Figure 16. A view of the cubic γ-brass structure combining standard and alternate $MgCu_2$-type fragments (Figure 14). a) Two standard $MgCu_2$-type fragments (red) separated from two alternate fragments (blue) by an interfacial cluster (purple). A pseudo C_2 axis passing through the interface cluster relates the standard and alternate clusters. b) The standard $MgCu_2$-type fragment representation can be extended past the interface. c) Likewise, the alternate representation can be carried past the interface. This combined viewpoint will be used to emphasize the structural relationship between the cubic γ-brass, $Cd_{0.213}Pd_{0.787}$, and $Cd_{0.235}Pd_{0.765}$ structures.

two representations can be thought of as inversion domains of each other. In γ-brass, such interfaces exist, but they are connected to one another only by pseudosymmetry (the representation shown in red is of perfect T_d symmetry; the blue representation is distorted from T_d symmetry). As we shall see, this twinning law is of great use in understanding both $Pd_{0.213}Cd_{0.787}$ and $Pd_{0.235}Cd_{0.765}$; for these systems the originally pseudo C_2 axes become true crystallographic operations.

The $Pd_{0.213}Cd_{0.787}$ and $Pd_{0.235}Cd_{0.765}$ structures: In the last section, we uncovered a twinning law present in γ-brass itself (Figure 16). In Figure 17a, we show that the same twinning law is present in the $Pd_{0.213}Cd_{0.787}$ structure. Using the same coloring scheme as the earlier figure, we show the occurrence of the same standard (red), alternate (blue) and interface (purple) $MgCu_2$-type clusters as found in the cubic γ-brass structure. However, there is an important difference: while in the cubic γ-brass structure the standard and alternate clusters are only related to each other by a pseudo C_2 axis, here the two sets of clusters are related through the chemical twinning of a true C_2 axis.

The clusters have been chosen following the calculated Mulliken populations. Atoms on adamantane and chair sites are electron rich, while those on the tetrahedron of tetrahedra (TOT) are electron poor. They are therefore the same clusters (drawn from a different perspective) as those derived from our previous $MgCu_2$ Laves analysis (see Figure 12). Within the framework of the twinning law, we now understand it is possible to create alternate assignments of the cluster atoms. In Figure 17b, we show a picture of the red representation, in which it has been extended to those previously blue clusters closest to the purple interface. Similarly, in Figure 17c, the blue representation is shown including the previously red clusters closest to the interface. As an

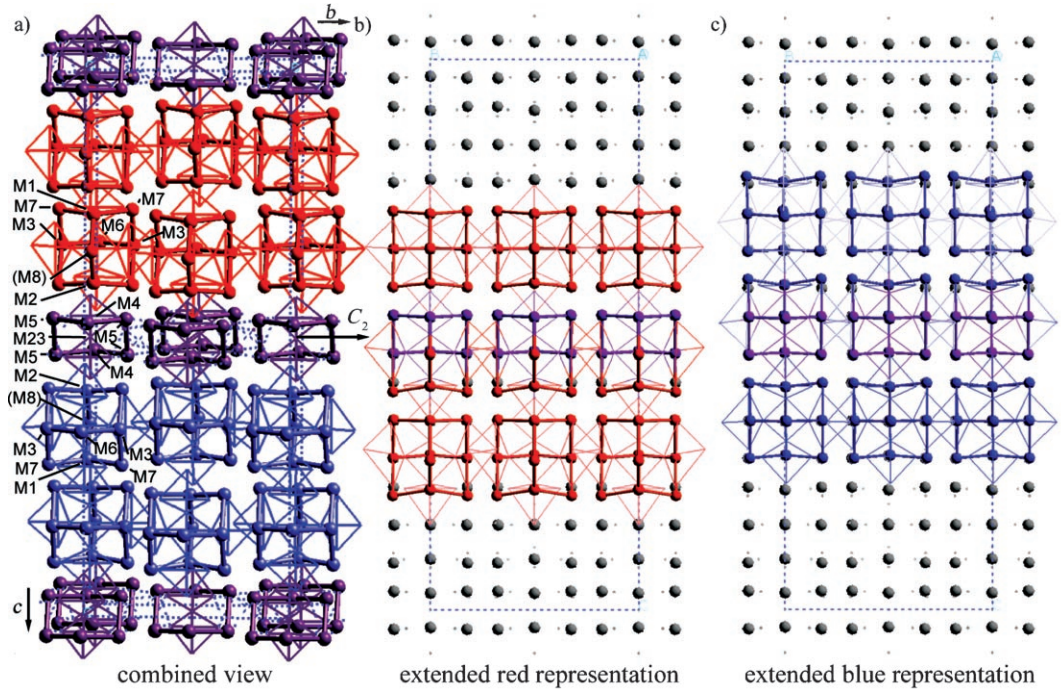

Figure 17. Multiple representations of the $Pd_{0.213}Cd_{0.787}$ structure, with its sites assigned to γ-brass clusters. a) The primary representation, consisting of the paired layers of γ-brass clusters separated by interface clusters (purple). Colors follow the convention of Figure 16. b) and c) Extended representations in which the representation regions are extended across the interface.

examination of this figure shows, all atom sites can be thought of in their primary representation (Figure 17a) and their twinned (or extended) representation (Figure 17b or c), with their twinned representation referring to the extended representation with respect to the closest interface to a given atomic site.

In Table 6, we classify all atoms by their primary and twinned representations. If in a given representation the atom lies on the three-coordinate adamantane site, two-coordinate adamantane site, outer TOT site, or inner TOT site, the site will be termed an OT, OH, CO, or IT site, respectively. Each position will therefore have at least two labels (one for both primary and twinned representations). Note that the nomenclature here is somewhat altered from the previous section. In the previous section, the labels OT, OH, CO, and IT referred to the four sites of the γ-brass structure. In this section they refer to the position on a cluster of an atom in a particular representation.

Table 6. Cluster atom types in primary and twinned representations.

$Pd_{0.213}Cd_{0.787}$	Cluster atom type[a]	$Pd_{0.235}Cd_{0.765}$	Cluster atom type[a]
M1	OT/OH	M1	OT/OT
M2	OT/OT	M2	OT/OT
M3	OT/OH	M3	OT/OH
M4	OT/OH	M4	OT/OH
M5	OT/OH	M5	OT/OH
M6	OH/OT	M6	OT/OH
M7	OH/OT	M7	OH/OT
M8	OH/CO	M8	OH/OT
M9	OH/CO	M9	OH/OT
M10	CO/OH	M10	OH/OT
M11	CO/OH	M11	OH/OT
M12	CO/CO	M12	OH/OT
M13	CO/IT-OH[b]	M13	OH/CO
M14	CO/CO	M14	OH/CO
M15	CO/CO	M15	OH/CO
M16	CO/CO	M16	OH/CO
M17	CO/IT	M17	CO/OH
M18	CO/IT	M18	CO/OH
M19	CO/IT	M19	CO/OH
M20	IT/CO	M20	CO/OH
M21	IT/CO	M21	CO/CO
M22	IT/IT	M22	CO/IT-OH[b]
M23	IT/IT	M23	CO/CO
		M24	CO/CO
		M25	CO/CO
		M26	CO/CO
		M27	CO/CO
		M28	CO/IT
		M29	CO/IT
		M30	CO/IT
		M31	CO/IT
		M32	IT/CO
		M33	IT/CO
		M34	IT/CO
		M35	IT/CO
		M36	IT/CO
		M37	IT/CO
		M38	IT/IT
		M39	IT/IT

[a] See Figure 4 for definition of atom labels. [b] Atom is equally close to two different interfaces and therefore has two possible extended representation assignments.

As this table shows, there is a direct correlation between atom site label and the calculated Mulliken charge population. We found earlier, for the cubic γ-brass structure, that of the four γ-brass sites, OT is most electron rich, followed by OH, then CO, and finally IT. The same trend is apparent in this table: the most electronegative sites are OT/OT sites, followed by OT/OH, OH/OT, OH/CO, CO/OH, CO/CO, CO/IT, IT/CO, and finally IT/IT sites. The main exceptions to these trends are the M13 site of $Pd_{0.213}Cd_{0.787}$ and the M22 site of $Pd_{0.235}Cd_{0.765}$. For these sites the atoms lie equally close to two different interfaces. Therefore, the atoms have representations in two different twinned representations. Taking into account these factors, the overall trend is maintained for these atoms as well.

Of particular interest in Table 6 are those sites that are either in OT or OH positions in *both* primary and twinned representations. Such atoms are fundamentally adamantane-like. For $Pd_{0.213}Cd_{0.787}$ and $Pd_{0.235}Cd_{0.765}$ these prove to be the M1–M7 and the M1–M12 positions, respectively. Comparison to Figure 10, Figure 11 shows that these sites are exactly those which belong either to the first bundle of most electronegative sites or the intermediate electronegativity sites. As the most electronegative sites are occupied by Pd atoms, while the occupation of the intermediate sites is perhaps primarily Cd, we need to find the factors that cause the intermediate sites to be less electronegative than other pure adamantane sites.

An examination of Figures 17 and 18 shows the difference between the intermediate sites (M7 for $Pd_{0.213}Cd_{0.787}$ and M12 for $Pd_{0.235}Cd_{0.765}$) and the most electronegative atoms. M7 ($Pd_{0.213}Cd_{0.787}$) and M12 ($Pd_{0.235}Cd_{0.765}$) are both sites that are OH in their primary representation, OT in their twinned representation, and which lie equally close to *two* interfaces. Therefore the Mulliken populations of the sites are influenced by a second interface. In both cases, using the second interface, these atoms prove to be CO atoms in this additional extended representation. Therefore, these sites have reduced adamantane character. With these facts in hand, we see the electronegativity of the M7 ($Pd_{0.213}Cd_{0.787}$) and M12 ($Pd_{0.235}Cd_{0.765}$) sites are reduced with respect to the most electronegative atoms.

We can now rationalize the twinning operations present in both $Pd_{0.213}Cd_{0.787}$ and $Pd_{0.235}Cd_{0.765}$. In these two structures, there are an insufficient number of Pd atoms to occupy all OT and OH sites of ordinary γ-brass. By introducing twinning operations, we reduce the number of sites that are OT and OH in both primary and twinned representations. The overall amount of twinning relates to the Cd–Pd content of the given system. Including the third representation further decreases this number. For nominal compositions $Pd_{0.213}Cd_{0.787}$ and $Pd_{0.235}Cd_{0.765}$ the percentage of sites which are adamantane-like in their primary, secondary, and (for atoms equally near two interfaces) tertiary representations are 23.2 and 24.1%, respectively, values loosely in accord with their nominal compositions.

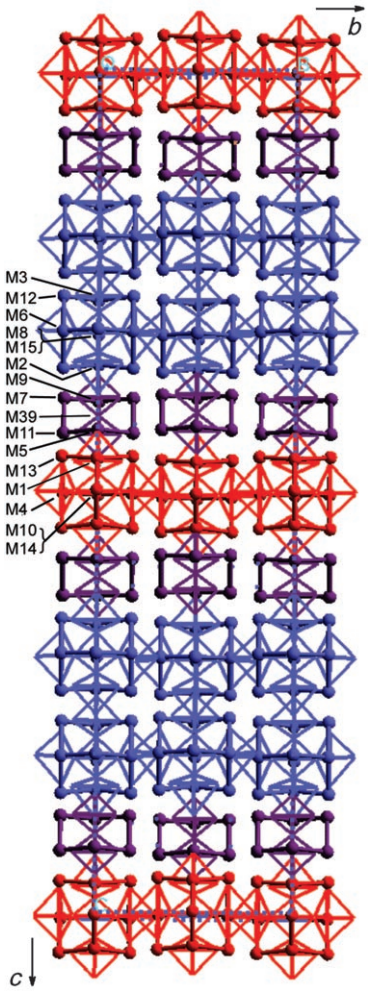

Figure 18. Combined view of the $MgCu_2$-type clusters in the $Cd_{0.235}Pd_{0.765}$ structure. See caption to Figure 17 for figure conventions.

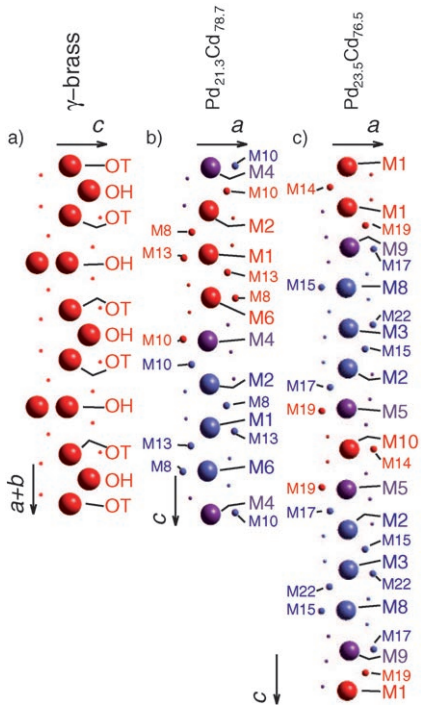

Figure 19. *S* and *L* chains in central planes of the unit cells a) γ-brass (the [1 1 0] plane), b) $Pd_{0.213}Cd_{0.787}$ (the $b=1/2$ plane), c) $Pd_{0.235}Cd_{0.765}$ (the $b=1/2$ plane). In a) red: standard representation. In b,c) colors refer to colors of atoms in Figures 17a and 18, respectively. Large spheres: adamantane atoms in both primary and twinned representation; intermediate spheres: partial adamantane-like character atoms; dots: TOT atoms in both primary and twinned representations.

Relation of composite and twinned pictures: So far we have developed two strikingly different pictures of γ-brass, $Pd_{0.213}Cd_{0.787}$, and $Pd_{0.235}Cd_{0.765}$. In the first view, we have shown how the three structures can be decomposed into chain sequences with varying *S* and *L* distances. In this picture, the difference between the different structure types lies in the varying ratios of *S* to *L*. In the view developed just above, we have considered a twinning operation that generates two different representations of the structure. This picture proves to account for the preferential site ordering in these structures.

We now seek to relate these two pictures. In Figure 19a, the *S* and *L* chains of γ-brass itself are re-drawn; the OT and OH atoms as given as spheres and IT and CO sites as points. (As in the earlier picture of *S* and *L* chains, only atoms which lie in the (1 1 0) plane itself are shown.) As Figure 19a shows, this *L* chain is solely comprised of OT and OH (spheres). By contrast, the *S* chains contains mainly CO and IT sites, and hence are primarily represented as points in the figure. However, with respect to the current discussion, a fraction of the *S* atomic sites are of OH character and are therefore represented as spheres.

In Figure 19b we consider the $b=1/2$ plane (equivalently the $b=0$ plane) of $Pd_{0.213}Cd_{0.787}$. In this picture one sees that the $b=1/2\,L$ chain continues to be composed only of OT and OH sites (and hence is seen as large spheres), but the *S* chains are not now large spheres. The *L* chain is comprised only of sites M1, M2, M4, and M6. These are exactly the sites that we believe to be principally Pd in character. By contrast *S* chain atoms contain either no adamantane character (represented as points) or adamantane character in only one of the two representations (represented as small spheres). No *S* chain site is occupied by Pd. Thus we see that for $Pd_{0.213}Cd_{0.787}$, both the *S*/*L* picture and the twinning picture are relevant to Pd and Cd site preferences.

A similar scenario unfolds for the $Pd_{0.235}Cd_{0.765}$ structure. The *L* chain continues to be composed only of adamantane sites, while none of the shown *S* chain sites are of pure adamantane character, Figure 19c (a picture again of $b=1/2$ atoms). We can relate these findings to Pd and Cd site preferences. As examination of Figure 19c shows that the $b=1/2\,L$ chain is composed of sites M1, M2, M3, M5, M8, M9, and M10, that is, almost the entire range of sites which are the most electronegative (i.e., have the highest Mulliken populations). As discussed earlier, following the nominal composition, the assessment of composition by microprobe,

and the refined single-crystal structure, it is this range of sites (M1–M11) that we believe are most likely principally occupied by Pd atoms.

Therefore, both the composite model and the twinning model inform us about different components of the atomic site preferences of the Cd and Pd atoms. The twinning model tells us which atoms are adamantane-like in the primary and secondary (and in some cases tertiary) representations. The composite model shows us that for the $b=0$ and $b=1/2$ atoms there is segregation of Pd atoms to the L chains and Cd atoms to the S chains. Both chemical twinning and the composite S/L descriptor appear fundamental to $Pd_{0.213}Cd_{0.787}$ and $Pd_{0.235}Cd_{0.765}$.

Conclusion

In this paper we have examined the $Pd_{1-x}Cd_x$, $0.755 \geq x \geq 0.800$ phases in general and $Pd_{0.213}Cd_{0.787}$ and $Pd_{0.235}Cd_{0.765}$ in particular. These phases prove to be variants of the γ-brass structure, and as such they add to the already rich field of γ-brass structural variants.[35,57,79–97] But they do more than just add another structure or two to the overall picture of γ-brass variants. Previous views of γ-brass focused on the polyhedral nature of the structure,[76,98] the fact that the γ-brass unit cell is a $3\times3\times3$ defective bcc lattice, the rhombohedral[83,89,99–101] or primitive[88,90,96,102] variants, or the $2\times2\times2$ superstructures of γ-brass.[91,103–108] More modern views of γ-brass have been of it as a cubic quasicrystalline approximant phase,[41,78,109] a view which highlights a six-dimensional view of the structure.[12,110]

The $Pd_{1-x}Cd_x$, $0.755 \geq x \geq 0.800$ variants of γ-brass bring to fore a new aspect of the parent phase, to wit, that γ-brass is a composite crystal composed of chains with two different periodicities: L and S. In γ-brass the S/L value is 5:3 (1.67). This becomes noteworthy as in $Pd_{1-x}Cd_x$, $0.755 \geq x \geq 0.800$ phases S/L varies from 1.61 to close to 1.64 (the former corresponding closely to both the golden mean and 21:13, and the latter value to 18:11). Indeed values of S/L between 1.64 and 1.67 may prove also to exist. As is well established, composite phases such as the $Pd_{1-x}Cd_x$, $0.755 \geq x \geq 0.800$ phases are (3+1)-dimensional systems. The space group names of such crystals have been systematized.[111] In the terminology of (3+1) space groups, $Pd_{0.213}Cd_{0.787}$ and $Pd_{0.235}Cd_{0.765}$ both may be characterized in superspace group $Xmmm(00\gamma)s00$ symmetry (equivalent to the standard superspace group $Fmmm(00\gamma)s00$).

At the same time, in trying to rationalize the $Pd_{1-x}Cd_x$, $0.755 \geq x \geq 0.800$ structures, we have been led to a twinning law underlying not just these phases, but γ-brass as well. The twinning law appears to be intimately connected to the Pd and Cd site preferences and to a connection to the even more fundamental Laves phase structure, $MgCu_2$. Thus we see a potential fundamental difference between the γ-brass parent structure and the $Pd_{1-x}Cd_x$, $0.755 \geq x \geq 0.800$ phases. The γ-brass structure is an electron compound with generally 21:13 valence s and p electrons per atom. By contrast, for both the $Pd_{0.213}Cd_{0.787}$ and $Pd_{0.235}Cd_{0.765}$ structures, the stoichiometric ratio of the Pd/Cd elements appears to play a role: $b=0$ and $b=1/2\,L$ chains are principally Pd-like, while $b=0$ and $b=1/2\,S$ chains are principally Cd-like. Thus in γ-brass, at all levels of calculation, we see a small number of states at the Fermi energy. By contrast, for $Pd_{0.213}Cd_{0.787}$ and $Pd_{0.235}Cd_{0.765}$ the number of states does not appear correlated to the varying valence electron numbers in these latter systems (see Supporting Information).

These points help clarify which new phases would be of interest for further structural characterization. On the one hand all six of the phase diagrams involving one Group 12 element (Zn or Cd) and one Group 10 element (Ni, Pd or Pt) show γ-brass variant structures. For only one of these systems has a single-crystal structure already been fully characterized ($NiZn_3$), and this structure, in hindsight, does appear to contain S and L chains.

Even more interesting, however, would be to examine those phases that, while potentially structurally related to $Pd_{0.213}Cd_{0.787}$ and $Pd_{0.235}Cd_{0.765}$, have fundamentally different stoichiometries from them. The interest here would be a single-crystal γ-brass derivative composed of Group 11 (Cu, Ag, or Au) and Group 12 (Zn or Cd) elements. To our knowledge, there are electron diffraction studies of such orthorhombic γ-brass derivatives, but as yet no single-crystal structures. Equally of interest would be ternary mixtures of the above elements. If stoichiometry does indeed play a role in structure stability, we may expect here different structures from those that we have previously obtained. Complex yet simple, three-dimensional crystals, higher dimensional composite crystals, or six-dimensional quasicrystal approximants, we feel certain only that γ-brass variants will continue to astound.

Acknowledgements

We are grateful for the financial support of the National Science Foundation (through grants DMR-007358 and DMR-0504703) and the Petroleum Research Fund. Use of the National Synchrotron Light Source, Brookhaven National Laboratory, was supported by the U.S. Department of Energy, Office of Science, Office of Basic Energy Sciences, under Contract No. DE-AC02-98CH10886. This work made use of the Cornell Center for Materials Research Facilities supported by the National Science Foundation under Award Number DMR-0079992. We are grateful for the assistance of John Hunt with the microprobe characterization, Dr. Emil Lobkovsky for assistance with single-crystal data collection, and Adrian C. So for his help in preparing the Supporting Information. We are grateful to Roald Hoffmann for discussions on other structures related to the $MgCu_2$-type (the $NaCd_2$ and α-Mn structures), and Dr. Lan-Feng Yuan for interesting us in the site preference problem in γ-brass. It has come to our attention that a rather similar set of phases has been recently uncovered by O. Gourdon and G. Miller at Iowa State. Note added in revision: During the review process this work has been published. See O. Gourdon, G. J. Miller, *Chem. Mater.* **2006**, *18*, 1848, and O. Gourdon, Z. Izaola, L. Elcoro, V. Petricek, *Phil. Mag.* **2006**, *86*, 419.

[1] I. W. Hamley, *The Physics of Block Copolymers*. Oxford University Press, Oxford (UK), **2003**.

[2] A. Vila-Sanjurjo, B.-S. Schuwirth, C. W. Hau, J. H. D. Cate, *Nat. Struct. Mol. Biol.* **2004**, *11*, 1054–1059.
[3] S. Samson, *Nature* **1962**, *195*, 259–263.
[4] S. Samson, *Acta Crystallogr.* **1965**, *19*, 401–413.
[5] S. Samson, *Acta Crystallogr.* **1967**, *23*, 586–600.
[6] "Crystal Chemistry of Transition Element Defect Silicides and Related Compounds"H. Nowotny in *The Chemistry of Extended Defects in Non-metallic Solids* (Eds.: L. Eyring, M. O'Keeffe), North-Holland, Amsterdam and London, **1970**, pp. 223–237.
[7] W. B. Pearson, *The Crystal Chemistry and Physics of Metals and Alloys*, Wiley-Interscience, New York, **1972**, pp. 676–699.
[8] A. J. Morton, *Phys. Status Solidi A* **1977**, *44*, 205–214.
[9] G. Novers, K. Schubert, *J. Less-Common Met.* **1980**, *75*, 51–63.
[10] Y. Yamada, S. Koh, *J. Phys. F* **1988**, *18*, 1371–1386.
[11] P. Villars, L. D. Calvert, *Pearson's Handbook of Crystallographic Data for Intermetallic Phases*, 2nd ed., ASM International, Materials Park, OH, **1991**.
[12] C. Janot, *Quasicrystals: A Primer*, Clarendon Press, Oxford, **1994**.
[13] N. Tamura, *Philos. Mag. A* **1997**, *76*, 337–356.
[14] H. Völlenkle, A. Wittmann, H. Nowotny, *Monatsh. Chem.* **1967**, *98*, 176–183.
[15] G. Flieher, H. Völlenkle, H. Nowotny, *Monatsh. Chem.* **1967**, *98*, 2173–2179.
[16] W. Jeitschko, E. Parthé, *Acta. Crystallogr.* **1967**, *22*, 417–430.
[17] R. Naslain, J. Etourneau, J. S. Kasper, *J. Solid State Chem.* **1971**, *3*, 101–111.
[18] D. Givord, P. Tenaud, J. M. Moreau, *J. Less-Common Met.* **1986**, *123*, 109–116.
[19] H. Lind, M. Boström, V. Petříček, S. Lidin, *Acta Crystallogr. Sect. B* **2003**, *59*, 720–729.
[20] A. J. Morton, *Phys. Status Solidi A* **1974**, *23*, 275–289.
[21] A. J. Morton, *Phys. Status Solidi A* **1976**, *33*, 395–403.
[22] A. J. Morton, *AIP Conf. Proc.* **1979**, *53*, 241–243.
[23] Y. Nakamura, H. Koike, O. Nittono, *Phys. Status Solidi A* **1990**, *118*, 389–400.
[24] Y. Koyama, J. Yoshida, H. Hoshiya, Y. Nakumura, *Phys. Rev. B* **1989**, *40*, 5378–5386.
[25] V. Demange, J. Ghanbaja, C. Beeli, F. Machizaud, J. M. Dubois, *J. Mater. Res.* **2004**, *19*, 2285–2297.
[26] S. Thimmaiah, M. Conrad, S. Lee, B. Harbrecht, *Z. Anorg. Allg. Chem.* **2004**, 630, 1762.
[27] A. J. Morton, *Phys. Status Solidi A* **1977**, *43*, K123 K125.
[28] H. Sato, R. S. Toth, *Phys. Rev.* **1961**, *24*, 1833–1847.
[29] A. Yamamoto, *Acta. Crystallogr. A* **1993**, *49*, 831–846.
[30] F. E. Rohrer, H. Lind, L. Eriksson, A.-K. Larsson, S. Lidin, *Z. Kristallogr.* **2000**, *215*, 650–660.
[31] F. E. Rohrer, H. Lind, L. Eriksson, A.-K. Larsson, S. Lidin, *Z. Kristallogr.* **2001**, *216*, 190–198.
[32] G. Lu, S. Lee, J. Lin, L. You, J. Sun, J. T. Schmidt, *J. Solid State Chem.* **2002**, *164*, 210–219.
[33] N. F. Mott, H. Jones, *The Theory of the Properties of Metals and Alloys*, Dover, New York, NY, **1958**, p. 168.
[34] W. Hume-Rothery, *Electrons, Atoms, Metals and Alloys*, Dover, New York, **1963**.
[35] L. M. Hoistad, S. Lee, *J. Am. Chem. Soc.* **1991**, *113*, 8216–8220.
[36] J. K. Burdett, *Chemical Bonding in Solids*, Oxford University Press, New York and Oxford, **1995**, pp. 285–287.
[37] A. T. Paxton, M. Methfessel, D. G. Pettifor, *Proc. R. Soc. London Ser. A* **1997**, *453*, 1493–1514.
[38] XPREP, Version 5.1. Bruker Nonius, Madison, Wisconsin (USA), **1997**.
[39] V. Petříček, M. Dusek, L. Palatinus, Jana2000, the crystallographic computing system, Institute of Physics, Praha (Czech Republic), **2000**.
[40] O. Masson, E. Doorhée, A. N. Fitch, *J. Appl. Crystallogr.* **2003**, *36*, 286–294.
[41] U. Mizutani, T. Takeuchi, H. Sato, *J. Non-Cryst. Solids* **2004**, 334/335, 331–335.
[42] U. Mizutani, T. Takeuchi, H. Sato, *Prog. Mater. Sci.* **2004**, *49*, 227–261.
[43] J. K. Burdett, E. Canadell, T. Hughbanks, *J. Am. Chem. Soc.* **1986**, *108*, 3971–3976.
[44] G. J. Miller, *Eur. J. Inorg. Chem.* **1998**, 523–536.
[45] C. S. Lee, G. J. Miller, *Inorg. Chem.* **2001**, *40*, 338–345.
[46] R. W. Henning, J. D. Corbett, *J. Alloys Compd.* **2002**, *338*, 4–12.
[47] G. Kresse, J. Hafner, *Phys. Rev. B* **1993**, *47*, 558–561.
[48] G. Kresse, J. Hafner, *Phys. Rev. B* **1994**, *49*, 14251–14269.
[49] G. Kresse, J. Furthmüller, *Comput. Mater. Sci.* **1995**, *6*, 15–50.
[50] G. Kresse, J. Furthmüller, *Phys. Rev. B* **1996**, *54*, 11169–11186.
[51] L. Arnberg, *Acta Crystallogr. B* **1980**, *36*, 527–532.
[52] H. J. Monkhorst, J. Pack, *Phys. Rev. B* **1976**, *13*, 5188–5192.
[53] D. Vanderbilt, *Phys. Rev. B* **1990**, *41*, 7892–7895.
[54] G. A. Landrum. YAeHMOP is freely available on the WWW at URL: http://sourceforge.net/projects/yaehmop/.
[55] P. Alemany, S. Alvarez, unpublished work cited in an unpublished table of eH parameters compiled by S. Alvarez, Universitat de Barcelona, **1993**.
[56] A. Bradley, P. Jones, *J. Inst. Met.* **1933**, *51*, 131–162.
[57] E. A. Lord, S. Ranganathan, *J. Non-Cryst. Solids* **2004**, 334/335, 121–125.
[58] Indeed, our choice of the letters *S* and *L* is to highlight the similarity of these crystals to the one-dimensional quasicrystal based on segments of length *S* and *L*.
[59] R. Herz-Fischler, *A Mathematical History of the Golden Number*, Dover, New York, **1998**.
[60] G. M. Sheldrick, SHELXS-97, Program for crystal structure solution; SHELXL-97, Program for crystal structure refinement, University of Göttingen, Göttingen (Germany), **1997**.
[61] D. C. Fredrickson, S. Lee, R. Hoffmann, J. Lin, *Inorg. Chem.* **2004**, *43*, 6151–6168.
[62] D. C. Fredrickson, S. Lee, R. Hoffmann, *Inorg. Chem.* **2004**, *43*, 6159–6167.
[63] P. M. Clark, S. Lee, D. C. Fredrickson, *J. Solid State Chem.* **2005**, *178*, 1269–1283.
[64] J. E. Huheey, *Inorganic Chemistry*. Harper and Row, New York, **1978**.
[65] K. H. Lieser, H. Witte, *Z. Metallkd.* **1952**, *43*, 396–401.
[66] P. Bagnoud, P. Feschotte, *Z. Metallkd.* **1978**, *69*, 114–120.
[67] T. Ohba, Y. Kitano, Y. Komura, *Acta Crystallogr. Sect. C* **1984**, *40*, 1–5.
[68] There is a single site, M15, which is not shown in either the 26- or 13-atom cluster. Within the Laves framework, it can be thought of as one of the missing TOT atoms on two adjacent 13-atom clusters.
[69] F. Garcia-Gonzales M. Meulemans, P. Delavignette, S. Amelinckx, *Mater. Res. Bull.* **1970**, *5*, 1025–1029.
[70] R. De Ridder, S. Amelinckx, *Mater. Res. Bull.* **1971**, *6*, 1223–1234.
[71] M. Snykers, R. Serneels, P. Delavignette, R. Gevers, S. Amelinckx, *Cryst. Lattice Defects* **1972**, *3*, 99–101.
[72] B. G. Hyde, A. N. Bagshaw, S. Andersson, M. O'Keeffe, *Annu. Rev. Mater. Sci.* **1974**, *4*, 43–92.
[73] P. Goodman, A. J. Morton, *Acta Crystallogr. Sect. A* **1982**, *38*, 848–854.
[74] D. Broddin, G. Van Tendeloo, J. Van Landuyt, S. Amelinckx, R. Portier, M. Guymont, A. Loiseau, *Philos. Mag. A* **1986**, *54*, 395–419.
[75] H. Q. Ye, S. Amelinckx, *J. Solid State Chem.* **1986**, *61*, 8–39.
[76] B. G. Hyde, S. Andersson. *Inorganic Crystal Structures*, Wiley, New York, **1989**.
[77] Y. Koyama, M. Hatana, M. Tanimura, *Phys. Rev. B* **1996**, *53*, 11462–11468.
[78] V. Demange, J. Ghanbaja, F. Machizaud, J. M. Dubois, *Philos. Mag.* **2005**, *85*, 1261–1272.
[79] B. Harbrecht, S. Thimmaiah, M. Armbrüster, C. Pietzonka, S. Lee, *Z. Anorg. Allg. Chem.* **2002**, *628*, 2744–2749.
[80] H. Flandorfer, *J. Alloys Compd.* **2002**, *336*, 176–180.
[81] D. Swenson, *Mater. Res. Soc. Symp. Proc.* **1997**, *453*, 367–372.

[82] G. A. Marking, H. F. Franzen, *J. Am. Chem. Soc.* **1993**, *115*, 6126–6130.
[83] E. H. Kisi, J. D. Browne, *Acta Crystallogr. Sect. B* **1991**, *47*, 835–843.
[84] Q. B. Yang, S. Andersson, *Acta Crystallogr. Sect. B* **1987**, *43*, 1–14.
[85] W. B. Pearson, *Z. Kristallogr.* **1981**, *156*, 281–294.
[86] L. Arnberg, S. Westman, *Z. Kristallogr.* **1980**, *152*, 103–108.
[87] H. Nyman, S. Andersson, *Acta Crystallogr. Sect. A* **1979**, *35*, 580–583.
[88] J. K. Brandon, H. S. Kim, W. B. Pearson, *Acta Crystallogr. Sect. B* **1979**, *35*, 1937–1944.
[89] J. K. Brandon, W. B. Pearson, P. W. Riley, *Acta Crystallogr. Sect. B* **1977**, *33*, 1088–1095.
[90] J. K. Brandon, R. Y. Brizard, W. B. Pearson, D. J. N. Tozer, *Acta Crystallogr. Sect. B* **1977**, *33*, 527–537.
[91] M. H. Booth, J. K. Brandon, R. Y. Brizard, C. Chieh, W. B. Pearson, *Acta Crystallogr. Sect. B* **1977**, *33*, 30–36.
[92] W. B. Pearson, J. K. Brandon, R. Y. Brizard, *Z. Kristallogr.* **1976**, *143*, 387–416.
[93] J. K. Brandon, P. C. Chieh, W. B. Pearson, P. W. Riley, *Acta Crystallogr. Sect. A* **1975**, *31*, 236–240.
[94] J. K. Brandon, R. Y. Brizard, P. C. Chieh, R. K. McMillan, W. B. Pearson, *Acta Crystallogr. Sect. B* **1974**, *30*, 1412–1417.
[95] D. Michell, A. J. Morton, A. P. Smith, *Phys. Status Solidi A* **1971**, *5*, 341–347.
[96] H. Ljung, S. Westman, *Acta Chem. Scand.* **1970**, *24*, 611–617.
[97] O. Heidenstam, A. Johansson, S. Westman, *Acta Chem. Scand.* **1968**, *22*, 653–661.
[98] W. B. Pearson, *The Crystal Chemistry and Physics of Metals and Alloys*, Wiley-Interscience, New York, **1972**.
[99] A. J. Bradley, S. S. Lu, *Z. Kristallogr. Kristallgeom. Kristallphys. Kristallchem.* **1937**, *90*, 20–37.
[100] T. Lindahl, Å. Pilotti, S. Westman, *Acta Chem. Scand.* **1968**, *22*, 748–752.
[101] T. Lindahl, S. Westman, *Acta Chem. Scand.* **1969**, *23*, 1181–1190.
[102] S. Westman, *Acta Chem. Scand.* **1965**, *19*, 1411–1419.
[103] A. Johansson, S. Westman, *Acta Chem. Scand.* **1970**, *24*, 3471–3479.
[104] L. Arnberg, A. Jonsson, S. Westman, *Acta Chem. Scand. A* **1976**, *30*, 187–192.
[105] R. Nesper, H. G. von Schnering, *J. Solid State Chem.* **1987**, *70*, 48–57.
[106] W. Hornfeck, S. Thimmaiah, S. Lee, B. Harbrecht, *Chem. Eur. J.* **2004**, *10*, 4616–4626.
[107] S. Lidin, M. Jacob, A. K. Larsson, *Acta Crystallogr. Sect. C* **1994**, *50*, 340–342.
[108] S. Thimmaiah, K. W. Richter, S. Lee, B. Harbrecht, *Solid State Sci.* **2003**, *5*, 1309–1317.
[109] S. Ranganathan, A. Subramaniam, A. P. Tsai, C. Dong, *Ferroelectrics* **2001**, *250*, 201–206.
[110] W. Steurer, *Z. Kristallogr.* **2004**, *219*, 391–446.
[111] *International Tables for Crystallography Volume C: Mathematical, Physical, and Chemical Tables* (Ed.: A. J. C. Wilson), Kluwer Academic, Boston, **1992**, pp. 797–844.
[112] SAINT, Bruker AXS, Madison, Wisconsin (USA), **1998**.
[113] X-RED, data reduction program, revision 1.02, Stoe & Cie, **1996**.
[114] X-SHAPE-crystal optimization for numerical absorption correction, revision 2.01, Stoe & Cie, **1996**.
[115] C. J. Bradley, A. P. Cracknell, *The Mathematical Theory of Symmetry in Solids*, Oxford University Press, London, **1972**, p. 109.
[116] R. E. Marsh, *Acta Crystallogr.* **1954**, 7, 379.
[117] H. W. Baird, F. A. Muller, *J. Biomed. Mater. Res.* **1969**, *3*, 375–382.
[118] C. W. Fairhurst, J. B. Cohen, *Acta Crystallogr. Sect. B* **1972**, *28*, 371–378.
[119] L. Arnberg, S. Westman, *Acta Crystallogr. Sect. A* **1978**, *34*, 399–404.

Received: January 31, 2006
Revised: July 7, 2006
Published online: November 8, 2006

